Revisiting the Ultrafast IR Spectroscopic Study of Free Volume Elements in Polymers: The Role of Probe Molecule's Internal Rotational Fluctuation in Anisotropy Decays

Saptarsi Mondal[a,b], Sourav Palchowdhury[a,b], Kwanghee Park[a,b], Soyeon Sung[b], Yong Ho Lee[b,*], Kyungwon Kwak[a,b,*], Minhaeng Cho[a,b,*]

[a] Center for Molecular Spectroscopy and Dynamics, Institute for Basic Science (IBS), Seoul 02841, Republic of Korea; [b] Department of Chemistry, Korea University, Seoul 02841, Republic of Korea

Abstract. Free volume in amorphous polymer materials is a crucial factor that dictates their macroscopic properties. By probing the orientational relaxation dynamics of an infrared probe embedded in the polymer matrix, the free volume element size and its probability distribution can be derived. Two distinct timescales of anisotropy decay of the nitrile probe in phenyl selenocyanate at ~10 and ~200 ps were assigned to two different wobbling-in-a-cone (WIAC) motions of the probe. In this study, using ultrafast infrared pump-probe (IR-PP) spectroscopy and molecular dynamics (MD) simulation, we investigate the rotational dynamics of phenyl selenocyanate (PSC), 2-methylphenyl selenocyanate (MPSC), and 2,2-dimethylphenyl selenocyanate (DMPSC) embedded in poly (methyl methacrylate) (PMMA), poly (2-phenoxyethyl acrylate) (PPEA) and poly (2-methoxyethyl acrylate) (PMEA) polymers to unravel the role of the internal rotational fluctuation of the nitrile group around the C(Ph)-Se(CN) bond vector on the rotational anisotropy as well as their biocompatible properties. We show that with increasing the steric effect by one or two methyl groups substituted at the ortho positions of the phenyl ring, the short-time rotational anisotropy dynamics of the nitrile group becomes 5-6 times slower in MPSC (28.7 ± 1.4) and DMPSC (31.9 ± 1.8) compared to that in PSC (4.8 ± 0.5 ps), and the corresponding amplitude decreases. These experimental observations indicate that the faster (~10 ps) rotational anisotropy component of phenyl selenocyanate in polymers originates from the internal rotational fluctuation of a nitrile group instead of a WIAC motion. The simulated dihedral fluctuation time-correlation functions of PMMA show that its segmental motions are substantially slower than the long-time component of rotational anisotropy by a factor of ~30-40, suggesting that the slow anisotropy decay component (~200 ps) reflects the static free volume element sizes in these polymers. This approach further reveals a larger free volume element size of 4.90 ± 0.04 Å for PPEA and 5.07 ± 0.04 Å in PMEA, having a longer sidechain length than that of PMMA (3.3 ± 0.03 Å), which could potentially impact the water permeability and hence biocompatibility of the respective polymers. Overall, the combined approach of IR pump-probe experiments, the discrete wavelet transform analysis method, and MD simulations employed in this study hold significant promise for investigating FVEs in various polymeric materials for potential biomedical applications.

1. Introduction

Free volume plays a significant role in determining the thermophysical properties and mechanical behaviors of polymers.[1-4] Polymers possess void spaces, referred to as free volume elements (FVEs), that originate from the inefficiency in packing and entanglement among the mesoscopic polymer chains in their amorphous form.[3-5] These regions are characterized by a lack of tightly packed polymer chains, providing empty spaces where other molecules or atoms can freely move.[2] The presence and arrangement of FVEs profoundly impact various aspects of polymer behavior, including mechanical properties, thermal expansion, electrical conductance, diffusion, permeability, and responsiveness to external stimuli.[5-13] The imperfect packing of amorphous polymer chains represents a non-equilibrium configuration where the polymer chains are effectively static, leaving polydisperse void spaces scattered inside the polymer matrix. Understanding the nature and characteristics of these FVEs is crucial for tailoring polymer materials with specific functionalities and improving their performance in various applications such as gas separation, membrane technologies, and drug delivery systems.[2] However, due to the sub-nanometric size (a few Å) of FVEs, it has been challenging to characterize the physical properties of FVEs experimentally.

Recently, the Fayer group demonstrated that the polarization-selective infrared pump-probe spectroscopy (IR-PP) can be used to extract the average size of FVEs in amorphous PMMA and polystyrene (PS) polymer by analyzing the anisotropic IR-PP signal of IR probe molecules embedded in the polymer matrix.[14, 15] They considered the nitrile (C≡N) stretch mode of phenyl selenocyanate (PSC) as an IR probe. Since the IR probe molecule in polymer does not assume all possible orientations with equal probability, the long-time anisotropy $r(\infty)$, which is related to the order parameter, does not decay to zero. Using the diffusion(wobbling)-in-a-cone (WIAC) model initially proposed by Kinosita et al.[16], they could connect the order parameters extracted from the anisotropy decay to the radii of FVEs fluctuating in different

timescales. The estimated FVE sizes in PMMA and PS were found to be in good agreement with those from the positron annihilation lifetime spectroscopy (PALS) experiments, even though a few critical assumptions had to be used to apply the WIAC model to describe the anisotropy decay of small IR probe molecules, PSC, located in void spaces of polymer matrices.[14, 15, 17-19] They further demonstrated that by using the IR-PP experiments, the ultrafast fluctuation time scale of FVEs could be measured, which cannot be achieved by using other approaches, including PALS.[14]

In previous studies, the two anisotropy decay components of the infrared (IR) probe, phenyl selenocyanate (PSC), in the polymers, whose time constants are approximately ~10 and ~200 ps, were attributed to two different WIAC motions. However, these studies did not consider the contribution of internal rotational fluctuation of the -SeCN moiety around the C(Ph)-Se(CN) bond on the measured anisotropy decay of the IR probe. The barrier height for such internal rotation was assumed to be similar to the thermal energy at room temperature so that the barrierless ultrafast rotation makes the resultant vector parallel to the unique axis of molecular rotation passing through the center of mass located near the C-Se bond and bisecting both the para-hydrogen and Se atom at the two ends. Nevertheless, other previous studies have reported that this type of internal rotation around a single bond could occur within a timescale of approximately 10 ps or a longer time, significantly affecting the overall rotational anisotropy of the molecule.[20, 21] Therefore, it is crucial to investigate whether the ~10 ps anisotropic IR-PP signal of the IR probe in the polymer is directly associated with the WIAC motion or internal rotational fluctuation because the calculated size of FVE will be affected too.

In this study, to systematically modulate the internal rotational barrier of the C≡N group, we synthesized 2-methylphenyl selenocyanate (MPSC) and 2, 2-dimethylphenyl selenocyanate (DMPSC) and examined the anisotropy dynamics of them embedded in PMMA polymer. Furthermore, we employed the discrete wavelet transform (DWT) method to remove the

scattering contribution from the IR-PP signal, which is beneficial for denoising the spectra, leading to a significant improvement in the signal-to-noise ratios of anisotropic IR-PP signals necessary for accurate quantitative estimations of FVEs and order parameters. Through a comparison of the orientational relaxation dynamics of ortho-substituted methyl derivatives of PSC molecules obtained from IR-PP measurements and molecular dynamics (MD) simulations, we observe a substantial change in the short-time (~10 ps) anisotropy dynamics of the respective IR probe, where the steric crowding at the ortho position of the phenyl ring significantly slows down the anisotropy decay. It strongly supports that the short-time decay reflects the internal rotational fluctuation of the C≡N group rather than the rotation of the whole IR probe molecule inside the cavity or void volume in a polymer.

Acrylate-based biocompatible polymers have been widely used as anti-biofouling coating materials in artificial organs, biomedical devices, and surgical instruments due to their exceptional ability to stay inert in physiological environments.[22-35] It has been observed that structurally similar therapeutic polymers could exhibit substantially different biocompatible behaviors when their plasma protein adsorptions or platelet adhesions are compared.[36-43] Therefore, considerable research has been carried out to identify the most crucial factors affecting the biocompatibility of those polymers.[23, 26, 42, 44-55] In our previous study, we used both polarization-selective IR pump-probe (IR-PP) and IR-visible photothermal imaging techniques to study water dynamics and distribution on the highly biocompatible PMEA and poorly biocompatible PPEA surfaces.[56] The IR-PP study of the adsorbed water on polymer surfaces revealed that both the sidechain functional group of the polymer and their mode of interaction with surrounding water molecules play a crucial role in dictating polymer biocompatibility. The IR-visible photothermal microscopy of the polymer surfaces revealed a considerable difference in the spatial distributions of water and the morphological features of these two polymers. Therefore, it is expected that the free volume elements (FVEs) of such

polymers could be different, which in turn would be the critical factor determining the gas or solvent permeability through the polymer matrix.[7, 11, 57-59]

We further compare the results obtained from the PSC probe in the PMMA polymer with those from poly (2-phenoxyethyl acrylate) (PPEA) and poly (2-methoxyethyl acrylate) (PMEA), which is expected to have larger FVEs due to a long sidechain functional group (-OCH_2CH_2OPh, and OCH_2CH_2OMe, respectively). PMMA is a strong hydrophobic polymer that does not show any biocompatible character. In contrast, PPEA is a weakly biocompatible material, and PMEA shows very strong biocompatibility and has been widely used commercially. This shows that the faster (~10 ps) rotational anisotropy of the IR probe does not undergo significant changes between different polymers. Overall, this study combines ultrafast IR-PP spectroscopy, DWT analysis, and MD simulation to provide detailed insights into how FVEs are sampled by the anisotropy dynamics of the probe molecule. We anticipate that these findings would significantly contribute to assigning and understanding the properties of different FVEs based on the probe molecules' orientational diffusion, culminate in their different macroscopic behavior.

2. Results and discussion

In this study, we consider the CN stretch mode of PhSeCN as the IR probe because its vibrational lifetime is substantially longer than other nitrile-derivatized compounds due to the so-called thermal insulation effect of the heavy atom, Se, that essentially decouples the CN stretch mode from the vibrational modes of the phenyl group.[60] The PSC-embedded polymer thin-film of three different polymers is shown schematically in Figure 1a. The detailed experimental methods of sample preparation, FT-IR, and IR-PP spectroscopy measurements are presented in Supplementary Note 1.

A. The origin of short-time anisotropy decay: Internal rotational fluctuation or WIAC motion?

To decipher the nature of the short-time orientational relaxation of the -Se–C≡N probe in a polymer matrix, whether this process is related to the internal rotational fluctuation of the -SeC≡N group around the C(Ph)-Se(CN) bond vector or WIAC motion, we synthesized 2-methylphenyl selenocyanate (MPSC) and 2,2-dimethylphenyl selenocyanate (DMPSC). The details of synthesis procedures can be found in section B of Supplementary Note 2. The chemical structures of PSC, MPSC, and DMPSC are shown in Figure 1a. The rotational anisotropy decay of the -SeCN probe inside the polymer is expected to be altered noticeably with increasing steric crowding at the phenyl ring's ortho position due to increased potential energy barriers if the internal rotational fluctuation is responsible for the short-time (~10 ps) anisotropy decay component. Here, we consider the CN stretch mode of -SeCN because its vibrational lifetime is substantially longer than other nitrile-derivatized compounds due to the so-called thermal insulation effect of the heavy atom, Se, that essentially decouples the CN stretch mode from the vibrational modes of the phenyl group.[60]

A.1. Potential energy surface (PES) scan for internal rotation

To calculate how increasing methyl substitution at the ortho position of the phenyl ring from PSC to DMPSC in PMMA polymer influences the barrier heights for the dihedral rotation of -SeCN probe around the C(Ph)-Se(CN) bond vector, we performed the potential energy surface scan (PES) in PMMA polymer at the MP2/6-311+G(D) level of theory (Figure 1b). Additionally, a brief discussion of the PES of the three IR probes in both the gas phase and in polymer calculated using different quantum chemical methodologies (B3LYP vs MP2), which seems to differ near the local minimum values of PES, along with the tentative reasoning behind this difference is provided in the Supplementary Note 1 for comparison. We employed the universal continuum solvation model based on the quantum mechanical electron density of

the solute cavity (SMD) via a set of overlapping spheres interacting with the continuum descriptor of the solvent generated from the dielectric constant, refractive index, and other key parameters as implemented in the Gaussian 16 quantum chemistry package[61] to represent the selenocyanate IR probe embedded in PMMA polymer matrix.[62] Although the SMD model is parametrized using an integral-equation-formalism polarizable continuum model (IEF-PCM) for bulk electrostatics, it is well known that the solvation free energy can be calculated accurately.[62] Figure 1b shows that the barrier height of internal rotation increases substantially with the methyl substitution at the ortho position of the phenyl ring. The estimated barrier height for the internal rotation for PSC in PMMA is about 0.85 kcal.mol^{-1}, which is larger than the room temperature thermal energy (0.59 kcal.mol^{-1}). However, this torsional barrier for PSC could be even higher if calculated using different methodologies, as shown in the supporting information. The higher torsional barrier than the room temperature indicates that the dihedral jump crossing the rotational barrier height is extremely rare, if not completely impossible (discussed later in the MD simulation part), suggesting that a significant dihedral population concentrated around the local minimum value of the PES of PSC stays within the potential well most of the time and can access the higher energy part of the PES due to thermal fluctuation at the nanoscopic polymer environment at room temperature. This suggests that the internal rotational fluctuation could potentially impact the overall anisotropy dynamics of the PSC probe inside the void space at this short timescale (~10 ps) as the dihedral jump crossing the torsional barrier could not be observed with a finite probability. The potential energy barriers for the internal rotation of -SeCN in MPSC and DMPSC embedded in PMMA polymer were calculated to be respectively 5.4 and 5.2 kcal.mol^{-1} at MP2/6-311+G(D) level of theory (but could be higher at different methodologies), which are, 6-7 times larger than that for the PSC. As the torsional energy barrier around the C(Ph)-C(Ph)-Se-CN shows a sharp increase with an increase in methyl substitutions from PSC to MPSC to DMPSC, to observe anisotropy decay

from the finite amount of internal rotation around the dihedral for MPSC and DMPSC requires much more energy that makes the process kinetically unfavorable. Therefore, the rotational anisotropy decay of the MPSC and DMPSC probe should be noticeably slower if it originates from the internal rotational fluctuation of the CN stretch mode.

A.2. FT-IR spectroscopy

The background subtracted and normalized FTIR spectra of the -SeCN probe of PSC, MPSC, and DMPSC in PMMA polymer are presented in Figure 1c, which indicates that with increasing -methyl substitution, the -SeCN stretch band is redshifted from 2155.0 cm^{-1} in PSC to 2154.0 and 2151.4 cm^{-1} in respectively MPSC and DMPSC molecule. Similarly, in highly polar dimethyl sulfoxide (DMSO) solvent, the CN stretch mode is redshifted from 2150.5 cm^{-1} for PSC to 2146.5 cm^{-1} for DMPSC, and even in nonpolar carbon tetrachloride (CCl_4) solvent, it undergoes a redshift from 2158.0 cm^{-1} for PSC to 2155.0 cm^{-1} for DMPSC (Figure S7). *Ab initio* harmonic frequency calculations of these IR probes in the gas phase as well as in solvent using the SMD solvation model utilizing the B3LYP functional and 6-311++G(d,p) basis set (Table S3) suggest that the redshift of the nitrile stretch mode with methyl substitution at the ortho position of the phenyl ring appears mainly due to the electronic structure change induced by the added methyl group, even though solvent polarity could slightly contribute to the observed redshift. The fitting parameters of the CN stretch band in polymers using Voigt functions, including the peak position, area, and FWHM, are tabulated in Tables S1 and S2 of Supplementary Notes 3 and 6, respectively, which suggests that the FWHM of the CN stretch band does not vary much for these molecules in the polymer environment.

A.3. IR-PP spectroscopy

A.3.1. Discrete wavelet transform analyses of the IR-PP spectra

The raw IR-PP spectra of PSC, MPSC, and DMPSC in PMMA are shown in Figures S3 and S4 of Supplementary Note 4 and Figure S8 of Supplementary Note 6, whereas PSC in PPEA and PMEA in Figure S5. Due to the intrinsic structural heterogeneity of polymer samples, pump-induced scattering fields interfering with the IR-PP signal field propagating in the direction of the probe beam make the signal-to-noise ratio (SNR) of experimentally measured IR-PP signal very low. This is especially so at long delay times (Figures S3 and S4), making it difficult to obtain the anisotropy decay profiles with high SNRs. Recently, we carried out IR-PP studies of acrylate-based polymer thin films to study the surface morphology and hydration structure, where the discrete wavelet transform (DWT)-based analysis methods were shown to be particularly useful for removing the contribution of pump-induced scattering fields from the IR-PP signal without distorting the spectra.[56] Employing the same multilevel one-dimensional wavelet decomposition algorithm (Supplementary Note 5 and reference 25), we could obtain the DWT-corrected IR-PP spectra corresponding to the 1-2 transition of the CN stretch band of different IR probes (Figures 2a-c).

A.3.2. Vibrational energy relaxation: Isotropic IR-PP signal

The lifetimes of the first excited vibrational state of the CN stretch mode of PSC, MPSC, and DMPSC embedded in the matrices of PMMA were measured by analyzing the isotropic IR-PP signals, $P_{iso}(t)$, which is defined as

$$P_{iso}(t) = \frac{I_{\parallel} + 2I_{\perp}}{3} \quad (1)$$

where $I_{\parallel}$ and $I_{\perp}$ are the parallel and perpendicular IR-PP signals (see section E of Supplementary Note 2 for details). Here, it should be noted that we focused on the excited-state absorptive IR-PP signals of the CN stretch mode instead of the 0-1 vibrational transitions

because the 0-1 transition signal originating from the sum of ground-state bleach and stimulated emission contributions is severely contaminated by the pump-induced heating term that overlaps with the 0-1 transition signal (Figures S3 and S4 of Supplementary Note 4). More specifically, we found that the IR-PP signal associated with the 0-1 vibrational transition decays more slowly due to the contribution of the increasing local heating term resulting from the vibrational energy dissipation of the excited CN stretch mode.

We next carried out global fitting analyses of the isotropic IR-PP signals (Figures S6e-f of Supplementary Note 5). We found that the isotropic IR-PP decays exponentially. The vibrational lifetimes of the excited CN stretch mode of PSC, MPSC, and DMPSC in PMMA are 423.3 ± 0.6, 587.1 ± 1.9, and 553.8 ± 2.4 ps, respectively (Table 1). Our experimental result (T= 423.3 ± 0.6 ps) for PSC in PMMA quantitatively agrees with that (434.0 ± 0.6 ps) reported by the Fayer group. Here, the deviation between the two values can be understood by noting that we performed the global fitting analyses of the 1-2 IR-PP signals of the CN probe, whereas Fica-Contreras et al. used the conventional single exponential fitting procedure of the 0-1 IR-PP signals.[14]

A.3.3. Rotational relaxation: Anisotropy decay

The anisotropy, $r(t)$, of the CN stretch mode of various IR probes in PMMA is determined by the difference between the parallel and perpendicular IR-PP signals as

$$r(t) = \frac{I_{\parallel}(t) - I_{\perp}(t)}{I_{\parallel}(t) + 2I_{\perp}(t)}. \quad (2)$$

The time dependence of $r(t)$ results from the motion of the IR probe, CN group, within the polymer. In general, $r(t)$ can be expressed in terms of a correlation function as

$$r(t) = \frac{2}{5}C_2(t) = \frac{2}{5}\langle P_2\big(\hat{\mu}(0)\cdot\hat{\mu}(t)\big)\rangle, \quad (3)$$

where $C_2(t) \equiv \langle P_2\big(\hat{\mu}(0) \cdot \hat{\mu}(t)\big)\rangle$, $P_2(x)$ is the second Legendre polynomial and the unit vector $\hat{\mu}(t)$ represents the orientation of the IR probe at time *t*. The angular bracket in Eq. (3) denotes an equilibrium average over the orientational distribution of the IR probe.

From the parallel and perpendicular IR-PP signals, we could obtain the time- and frequency-resolved $r\big(t, \omega_{pr}\big)$, where ω_{pr} is the probe beam frequency. In Figures 2d-f, the anisotropy decays at the 1-2 transition peak frequency of the CN stretch mode of different IR probes in PMMA are plotted. Their decaying time profiles could be quantitatively fitted with the following double exponential function with an instantaneously decaying component,

$$r\big(t, \omega_{pr}\big) = \frac{2}{5}[a_1(\omega_{pr})\delta(t) + a_2(\omega_{pr})\exp\{-t/t_1\,(\omega_{pr})\} + a_3(\omega_{pr})\exp\{-t/t_2\big(\omega_{pr}\big)\} + a_4\big(\omega_{pr}\big)], \quad (4)$$

where a_j are the normalized weighting factors, i.e., $\sum a_j = 1$, $\delta(t)$ is the Dirac delta function, and t_j are the decay time constants. Unless an appropriate model for the rotational relaxation of IR probe molecules in polymer matrices is introduced and used to analyze the anisotropy data, the relative amplitudes and decay time constants are just fitting parameters. As can be seen in Figures 2d-f, the initial anisotropy values are smaller than 2/5. The amount of initial drop of the IR-PP anisotropy from 0.4 reflects how much orientational dynamics of the probe molecule is missed in the current measurement with a pump laser pulse having a finite duration time. Also, the anisotropy does not decay to zero within the experimental time, so the constant offset, a_4, is needed to fit the anisotropy data, which indicates that the rotational relaxation of IR probe molecules is restricted in polymers. Furthermore, this limiting anisotropy provides information on the equilibrium orientational distribution of the probe.

The frequency-dependent anisotropy decay of the CN dipole moment vector obtained from the 1-2 pump-probe spectra of MPSC and DMPSC (Figures 2d-f) shows that the anisotropy decay at higher probe beam frequency becomes faster. The anisotropy decay

profiles at the corresponding center frequency of the excited vibrational state of the CN stretch band of PSC, MPSC, and DMPSC are directly compared in Figure 2h. It is clear that the anisotropy decays of MPSC and DMPSC become substantially slower at a short time regime than that of PSC in PMMA (Figure 2i).

Next, global fitting analyses on the anisotropic IR-PP signals of the excited vibrational state of the CN stretch mode were performed using the sum of exponential functions with a constant offset considering a wide spectral range of the 1-2 pump-probe spectra. The detailed fitting parameters associated with the rotational anisotropy decay at different probe beam frequencies are tabulated in Table S4 of Supplementary Note 6. The time constants of the short-time anisotropy decay components of MPSC and DMPSC in PMMA are 28.7 ± 1.4 ps and 31.9 ± 2.9 ps, respectively, which are ~ 6-7 times slower than that of PSC probe (Table 1). This dramatic slowdown of the short-time anisotropy dynamics of the CN stretch band with the addition of steric hindrance around -SeCN group in MPSC and DMPSC suggests that early-time anisotropy dynamics occurring at ~10-20 ps timescale is associated with the internal rotational fluctuation of the -SeCN moiety about the C(Ph)-Se bond vector as opposed to the WIAC motion. Furthermore, the long-time anisotropy dynamics of the CN group in MPSC and DMPSC also become, respectively, ~10 and 20% slower, which may be attributed to the increased moment of inertia by the substituted methyl group at the phenyl ring's ortho position. We calculated the principal components of inertia and van der Waal's volume of these IR probes (Table S8), which show that both properties increase from PSC to DMPSC, aligning well with the experimental findings.

The anisotropy decays for all three IR probes in PMMA can be decomposed to a fast component with ~10-20 ps time constant and a slow component with ~ 200 ps time constant, which suggests that there are at least two timescale-separated rotational relaxation processes. We found that the decaying pattern of anisotropy $r(t, \omega_{pr})$, in contrast to the isotropic signal,

depends on the probe beam's angular frequency ω_{pr} (see Figures 2d-2f and Table S4 of Supplementary Note 6). More specifically, the orientational relaxation dynamics probed at higher probe frequencies are fast in all three cases.[14, 15] We shall return to this experimental finding later in this paper.

A.4. Quantitative analyses of anisotropy decays

Kinosita et al.[16] and later Lipari and Szabo[63] developed a theory called diffusion(wobbling)-in-a-cone model to describe the fluorescence emission anisotropy of rod-shaped cylindrical fluorophore in a membrane. The probe is assumed to diffuse freely ("wobbles") within a cone of half-angle ϑ, which means that the equilibrium orientational distribution function with respect to the polar angle θ is a constant for $0 \leq \theta \leq \vartheta$ and zero otherwise. Due to the molecular symmetry, the orientational distribution function was assumed to be independent of the azimuthal angle. Similarly, as shown in references 14 and 15, the orientational relaxation dynamics of the CN group of PSC trapped inside the polymer matrix can be described as WIAC motions with varying timescales due to the spatial confinement and limited flexibility of polymer backbones and sidechains restricting the rotational motions of each probe molecule in a given free volume.

A.4.1. Inertial dynamics at short times

The experimentally measured initial anisotropy deviates from the ideal value of 0.4. This can be explained by noting that the inertial dynamics of the CN group is substantially fast, so it becomes impossible to measure its contribution to the short-time anisotropy decay with approximately 100 fs duration IR laser pulses. This inertial orientational relaxation of the IR probe can be modeled as a WIAC motion with approximately Dirac delta function-like decay, where the half-cone angle specifying the angular space of the inertial WIAC motion is denoted

as θ_{inert}. Since the diffusive (wobbling) motion in the range of polar angle, $0 \leq \theta \leq \theta_{inert}$ is free, the normalized orientational distribution function is

$$P_{inert}(\theta) = \frac{1}{2\pi\,(1 - cos\theta_{inert})} \qquad 0 \leq \theta \leq \theta_{inert}$$
$$= 0 \qquad otherwise. \tag{5}$$

Then, one can calculate the limiting anisotropy (see Ref. 54) and write the inertial contribution to $r(t)$ as

$$C_{2,inert}(t) = S_{inert}^2 + (1 - S_{inert}^2)\,\delta(t), \tag{6}$$

where the associated order parameter S_{inert} is given as

$$S_{inert} = \frac{1}{2} cos\theta_{inert}(1 + cos\theta_{inert}). \tag{7}$$

Note that the limiting anisotropy due to the inertial WIAC motion is S_{inert}^2. Therefore, the measurement of this order parameter provides direct information on the cone semiangle θ_{inert}, which determines the radius of the cone or the associated free volume element.

A.4.2. Internal rotation of CN group

The second component contributing to the anisotropy decay could be the internal rotational relaxation of the CN group in the IR probe molecules. The CN group can undergo an internal rotation around the single bond between the phenyl ring and the Se atom, which results in the decrease of $r(t)$. We need to calculate the contribution of such internal rotation to the limiting anisotropy $r(\infty)$. First, when the internal rotational degree of freedom is the only component making the anisotropy decay, the orientational distribution function $P_{ir}(\theta)$ can be approximately written as

$$P_{ir}(\theta) = \frac{1}{2\pi\, sin\theta_0}\,\delta(\theta - \theta_0), \tag{8}$$

where $2\pi\ sin\theta_0$ is the normalization constant. Secondly, using the property of correlation functions, from Eq. (4) one can write $r(\infty)$ as

$$r(\infty) = \frac{2}{5}\langle P_2(\cos\theta)\rangle^2. \tag{9}$$

The average of $P_2(\cos\theta)$ over $P(\theta)$ can be calculated so that the limiting anisotropy associated with this internal rotational relaxation is given as

$$r(\infty) = \frac{2}{5}(P_2(\cos\theta_0))^2. \tag{10}$$

Considering the chemical structure obtained from a MP2 level calculation of PSC, the angle θ_0, which is the angle between the bond axis of (Ph)C-Se and the CN bond axis, is approximately 72°. However, this angle (72°) should not be considered to calculate $r(\infty)$ with Eq. (10) because the phenyl group in PSC is not infinitely heavier than the CN group. Thus, the effective angle θ_0 could be smaller than 72° and could be estimated by measuring the limiting anisotropy $r(\infty)$ associated with this internal rotation experimentally together with Eq. (10).

The time-dependence of $r(t)$ resulting from the internal rotation of the CN group cannot be simply described by considering a diffusion equation of rotating objects in a two-dimensional space due to the presence of potential energy barriers along the internal rotational coordinate. Therefore, it is difficult to obtain an analytical expression for the time-dependent part of $r(t)$ in terms of the associated rotational diffusion constant, the viscosity of the local environment, and potential energy barrier heights. A convenient approximate expression for $r(t)/r(0)$ resulting from the internal rotational motion is an exponential function, i.e.,

$$C_{2,ir}(t) = (P_2(\cos\theta_0))^2 + (1 - (P_2(\cos\theta_0))^2)\exp(-t/t_{ir}), \tag{11}$$

where t_{ir} denotes the decay time constant associated with the internal rotational relaxation. Defining the associated order parameter as

$$S_{ir} = P_2(\cos\theta_0), \tag{12}$$

one can rewrite Eq. (11), similar to Eq. (6), as

$$C_{2,ir}(t) = S_{ir}^2 + (1 - S_{ir}^2)\exp(-t/t_{ir}). \tag{13}$$

A.4.3. Wobbling-in-a-cone motion of PSC as a rod-shaped object

If PSC molecules are in void spaces (FVEs) where they can freely wobble (diffuse) in a space approximated as a cone, and if the internal rotation of the CN group is much faster than this wobbling motion of PSC as a whole, we can treat a single PSC as a rigid rod with cylindrical symmetry. In this limiting case, one can assume that the effective vibrational transition dipole unit vector, which is the average of the CN group's $\hat{\mu}$ over $P_{ir}(\theta)$, is coaxial with the molecular axis parallel to the (Ph)C-Se bond vector. Therefore, the WIAC motion of a rod-shaped molecule is what we need to consider describing its contribution to $r(t)$. Using the standard WIAC model, one can immediately have

$$C_{2,fve}(t) = S_{fve}^2 + \left(1 - S_{fve}^2\right)\exp\left(-t/t_{fve}\right), \tag{14}$$

where t_{fve} is the average relaxation time constant of rod-shaped IR probe molecules in FVEs, and the corresponding order parameter is related to the cone half-angle of FVE as

$$S_{fve} = \frac{1}{2}cos\theta_{fve}\left(1 + cos\theta_{fve}\right). \tag{15}$$

A.4.4. Total anisotropy decay

In the above, we defined three different order parameters (see Eqs. (7), (12), and (15)) that are associated with varying types of reorientation processes. By definition, the order parameter represents the extent of anisotropy decay associated with each process. If the three relaxation processes occur independently from one another, one can write the total correlation function $C_2(t)$ as the product of the three correlation functions, i.e.,

$$
\begin{aligned}
C_2(t) &= C_{2,inert}(t)C_{2,ir}(t)C_{2,fve}(t) \\
&= \{S_{inert}^2 + (1 - S_{inert}^2)\,\delta(t)\} \times \\
&\{S_{ir}^2 + (1 - S_{ir}^2)\exp(-t/t_{ir})\} \times \\
&\{S_{fve}^2 + (1 - S_{fve}^2)\exp(-t/t_{fve})\}.
\end{aligned}
\tag{16}
$$

In the case when the two decay time constants are substantially different, i.e., $t_{ir} \ll t_{fve}$, one can rewrite Eq. (16) approximately as

$$
\begin{aligned}
C_2(t) \cong (1 - S_{inert}^2)\,\delta(t) + S_{inert}^2(1 - S_{ir}^2)\exp(-t/t_{ir}) \\
+ S_{inert}^2 S_{ir}^2(1 - S_{fve}^2)\exp(-t/t_{fve}) + S_{inert}^2 S_{ir}^2 S_{fve}^2.
\end{aligned}
\tag{17}
$$

Comparing this equation (17) with our fit function in Eq. (4), we find that the amplitudes of the four terms in Eq. (4) can be related to the order parameters as

$$
\begin{aligned}
a_1 &= 1 - S_{inert}^2 \\
a_2 &= S_{inert}^2(1 - S_{ir}^2) \\
a_3 &= S_{inert}^2 S_{ir}^2(1 - S_{fve}^2) \\
a_4 &= S_{inert}^2 S_{ir}^2 S_{fve}^2.
\end{aligned}
\tag{18}
$$

A.5. Simulated rotational anisotropy.

All-atom molecular dynamics simulation of various IR probes (PSC, MPSC, and DMPSC) embedded in PMMA polymer were performed using the fixed-charge non-polarizable CHARMM force field parameters[64] to gain detailed molecular level insights of different molecular processes associated with the rotational anisotropy of the IR probe inside polymer FVEs. The detailed methodology of such simulation is presented in Supplementary Note 8. The rotational anisotropy of the CN bond vector is expressed in terms of the second Legendre polynomial $C_2(t)$ as follows,

$$C_2(t) = \frac{\langle 3cos^2\theta - 1\rangle}{2}, \quad (19)$$

where θ is the angle made by the unit vector directing along the CN bond between two different time origins. Figure 3(a) compares the computed $C_2(t)$ among three experimentally investigated probes PSC, MPSC, and DMPSC. To eliminate the effect of molecular van der Waals volumes and the principal component of inertia of the probes on their computed rotational anisotropies (refer to SI Table), we performed additional simulations for a series of configurations of PSC whose torsional coefficients around the (Ph)C-(Ph)C-Se-CN dihedral were adjusted to mimic the potential energy barrier for DMPSC around the same dihedral while keeping the atomic site charges and Lennard-Jones parameters unchanged. We will refer to this particular PSC model as 'mimic DMPSC'. The computed $C_2(t)$ is fitted using a double exponential function with an instantaneously decaying component and a constant offset as Eq. 5. The δ(t)-component is obtained from a single exponential fit to the initial 1 ps component of $C_2(t)$. While fitting the TCFs by a double exponential function, the δ(t) -component is kept constrained. The fitted parameters for different probe molecules are tabulated in Table 2. Figure 3(a) shows that simulated $C_2(t)$ decays at a slower rate as the number of ortho-substituted methyl groups increases from PSC to DMPSC. The τ_1 values tabulated in Table 2, which correspond to the faster dynamics of the vibrational probe, are in good agreement with the experimental values. For the mimic DMPSC model, $C_2(t)$ falls at a slower rate than that in PSC, yielding a τ_1 value twice as larger as PSC. The dihedral angle (C(Ph)-C(Ph)-Se-CN) distribution of the PSC and mimic DMPSC is illustrated in Figure S10. A significantly narrower dihedral distribution for mimic DMPSC compared to that for PSC suggest that a larger fraction of the dihedral population is likely to be concentrated around the local minimum value of the PES at approximately 90°. Therefore, the internal rotational fluctuation of the dihedral in mimic DMPSC could sample a smaller angular space than that in PSC. Consequently, anisotropy decay from this larger fraction of the population clustering around

the equilibrium dihedral angle position in mimic DMPSC leads to a kinetically unfavorable process resulting in a slower time constant observed in the mimic DMPSC compared to PSC. This aspect is also evident from the fitting analyses of both experimental and simulated TCFs, where the contribution of the internal rotational fluctuations on the rotational anisotropy decay (pre-exponential factor of the faster anisotropy decay timescale) decreases with increasing -methyl substitution. So, an increase in the torsional barrier, either by increasing steric crowding at the ortho positions of the phenyl ring (DMPSC > MPSC > PSC) or by tweaking the torsional parameters (mimic DMSPC), hinders the motion of the SeCN unit around the (Ph)C-Se bond. Although simulated time constant, τ_2, associated with the slow component, matches well with the experimental values for PSC and MPSC, it is two times larger than the experimental value for DMPSC. This discrepancy could be understood by noting the limitation of force field-based simulations. We simulated DMPSC with a different set of force field parameters, resulting in the τ_2 value close to the experiment. However, such a new simulation yields τ_1 to be 1.5 times larger than the experiment (Supplementary Note 8). We should note that the τ_2 value for mimic DMPSC is almost twice that of PSC. This observation suggests a difference in the magnitude of mean-squared torques experienced by a flexible PSC compared to its conformationally more rigid analog, the mimic DMPSC. Additionally, the long-time slowing down of the rotational anisotropy also indicates a possible coupling of rotational dynamics in these two timescales. In other words, the rotational anisotropy at short times is not decoupled with the anisotropy decay at longer times as well.

Further, to decouple the timescale of the internal rotation of the -SeCN unit around the (Ph)C-Se bond from the overall molecular rotation, a set of simulations was performed with PSC, MPSC, and DMPSC, where the phenyl ring atoms were kept frozen (by initializing the ring atom velocity components to zero as well as setting the computed force components on each of the ring atoms at each time step to zero), while the remaining bath atoms (polymer and

SeCN unit) are allowed to move. The computed $C_2(t)$ of the CN bond vector from such simulations are shown in Figure 3(b), which shows an oscillatory behavior from 20 ps onward, reflecting the limiting value of $C_2(t)$ due to internal rotation. Such TCFs are fitted with a damped oscillator model,

$$C_2(t) = a_1\delta(t) + a_2 e^{-t/\tau_1} cos\left(\frac{2\pi t}{T} - \phi\right) + a_3, \quad (20)$$

where T and φ are the period and phase angle, respectively. Although the complete set of fit parameters can be found in Table S6 of Supplementary Note 8, τ_1 values are mentioned within parenthesis in Table 2. The $C_2(t)$ in Figure 3 decays at a slower rate with the increase in steric crowding at the ortho positions of the phenyl ring, analogous to the fully flexible model of the probes. The tabulated τ_1 values of this frozen ring model are quite close to the fully flexible model of a given probe. Consequently, the anisotropy decay observed in the MD simulation leading to the limiting anisotropy a_3, occurs solely due to the internal rotational fluctuation. The value of this limiting anisotropy a_3 corresponds to a semiangle of approximately 18.0°, which closely matches the experimentally obtained $\langle\theta_{ir}\rangle$ (=18.3°). These observations, together with the ultrafast IR PP experimental results, suggest that the internal rotation of the SeCN unit around the (Ph)C-(Ph)C-Se-CN dihedral is the major contributor to the faster timescale of the rotational anisotropy decay of the CN group in all three IR probe molecules.

B. Is polymer segmental dynamics relevant within the experimental observation window?

According to the previous study, the τ_2 values in Table 2 were concluded to be related to the probe rotation in the second diffusive cone of the WIAC model, which originates from the constraint release of polymer backbone rearrangements on a timescale larger than τ_1. We attempted to characterize the timescales of polymer structural relaxation in terms of fluctuations in dihedral angle [φ(t)] TCFs of the polymer backbone.

$$C_\phi(t) = \frac{\langle cos\phi(t) cos\phi(0)\rangle - \langle cos\phi(0)\rangle^2}{\langle cos^2\phi(0)\rangle - \langle cos\phi(0)\rangle^2}, \quad (21)$$

and reorientational TCFs ($C_1(t) = \langle \cos\theta \rangle$) of side chains. Figure 3(c) shows computed TCFs associated with different dihedrals and sidechains of the PMMA polymer. The dihedrals are chosen as having at least one polymer backbone atom, whereas side chain vectors correspond to carbonyl and methoxy units (see the inset of Figure 3(c)). We observe that TCFs in Figure 3c only decay up to 3-7% in an observation period of 10 ns. The computed TCFs are fitted using a tri-exponential equation, and the fit parameters are tabulated in Table S7 of Supplementary Note 8. The calculated faster sub-diffusive fluctuations in the TCFs occur at a timescale >200 ps, whereas the longer time relaxation occurs at a timescale of 5-7 ns. The computed translational diffusion coefficient of monomer residues in the PMMA chain is also found to be small ($D = 1.17E{-}14\ m^2s^{-1}$), ensuring an average diffusion length in the timescale of τ_2 will be <0.05 Å. The superposition of snapshots corresponding to the initial polymer chain configuration (0 fs, red) and final simulated configuration (10 ns, purple) of around 6Å from the PSC molecule is presented in Figure 3d, which shows that the polymer backbone motion is extremely limited. This observation again suggests relatively insignificant polymer segmental dynamics.

Based on these timescales of PMMA segmental relaxation, we can safely assume that the τ_2 values in Table 2 are hardly affected by the constraint release mechanism of polymer structure. Furthermore, the timescale of the inertial dynamics obtained from the fitting of the simulated TCF of the IR probe for frozen phenyl ring approximation, where only inertial relaxation and internal rotation can occur, matches pretty well with that obtained from the flexible geometry of the vibrational probes in PMMA. The similar timescale of the inertial relaxation dynamics for both flexible and frozen-ring model suggest that the instantaneous inertial dynamics mainly originates from the motion of the -SeCN moiety about the C(Ph)-Se bond vector.

C. Proposed Model

Combined experimental and computational findings indicate that the faster rotational anisotropy dynamics of the PSC probe within ~10 ps timescale is associated with instantaneous inertial dynamics and internal rotational fluctuation of the -SeCN unit, which collectively sample the angular space around it, as pictorially represented in violet in Figure 4. However, we would like to emphasize that this free space may not encompass the entire physically realizable free volume elements (FVE) as conventionally understood but rather represents only a portion of it. Though, we should acknowledge that the current evidence might be insufficient to assert that the faster rotational anisotropy is solely a result of internal rotational fluctuation. There is a fair probability that early-time wobbling motion may also contribute to the anisotropy decay. This early-time WIAC motion may be particularly relevant for certain IR probes which lack internal rotational fluctuation but still exhibit biexponential anisotropy decay. Recent findings using time-resolved infrared spectroscopy of 1,2-disubstituted ethyl radical derivatives indicate that the gauche-to-anti isomerization reaction involving carbon-carbon single bond rotation at room temperature occurs with a very slow timescale of about 35-45 ps.[21] Hence, we propose that the fast rotational anisotropy decay is governed by a more intricate relaxation mechanism involving primarily internal rotational fluctuation and wobbling-in-a-cone (WIAC) motion to some extent. These processes might also influence each other. This finding highlights the complexity of rotational dynamics in specific systems and suggests that when internal rotational fluctuation is present and the barrier height is higher than room temperature energy, it can predominantly influence the short-time anisotropy dynamics of the probe molecules inside the polymer.

Note that the simulated TCFs corresponding to the segmental relaxation of PMMA polymer decay just about 1% within ~200 ps timescale, indicating that the WIAC-type diffusive dynamics of the IR probe has not started yet within this regime. The longer time

rotational anisotropy decay of the PSC probe in PMMA at ~ 200 ps timescale, which is associated with the WIAC motion, probes the available angular space depicted in cyan color in Figure 4. This angular space virtually does not change in size and shape within this time regime as supported by the MD simulation, unlike the previous study where the longer timescale (~200 ps) anisotropy decay of the PSC probe was assigned to the FVE size and shape fluctuation inside the polymer matrix due to the constraint release mechanism of FVE involving structural rearrangement of the sidechain functional group. Our study shows that long timescale orientational relaxation of the PSC probe reports the static FVEs of the polymer (Figure 4).

However, to ensure a more accurate analysis of the FVE size and distribution, it becomes crucial to develop and utilize IR probes that do not have any internal rotation but have a long vibrational lifetime. Such probes will provide a clearer picture of the long-time WIAC motion, which likely samples the static FVEs of the polymer. In essence, we aim to convey that the initial void space sampled by internal rotational fluctuation is, probably, irrelevant to the actual physical FVEs of the polymer, which can only be sampled by the long-time WIAC motion.

D. Anisotropic IR-PP signal of CN of PSC in PMMA, PPEA, and PMEA

Next, we compare the anisotropic IR-PP signal of the CN stretch mode of PSC in PMMA to that in PPEA and PMEA to understand the role of an increased sidechain functional group of PPEA on the rotational anisotropy of the IR probe. The FT-IR spectra of the CN stretch mode of PPEA and PMEA undergo a redshift of 2.1 and 1.8 cm^{-1}, respectively, compared to that of PMMA (Figure 5b), suggesting that the electrostatic environment around the IR probes are different. Figure 5d shows the frequency-dependent anisotropy decay of the excited CN transition band (1-2) of PSC in PPEA and PMEA.

The global fitting analysis of the frequency-dependent anisotropy decay of the PSC in PMMA, PPEA, and PMEA was performed using Eq. (4) and (18), which results in the time

constants t_{ir}, and t_{fve} and the three different order parameters, S_{inert} (inertial relaxation), S_{ir} (short time internal rotation), and S_{fve} (long time WIAC motion) (Table S5 of Supplementary Note 7). We considered the IR-PP signal of the CN stretch mode starting from 0.2 ps for analysis as the dynamics prior to that is complicated and obscured by the perturbed free induction decay originating from the coherent interaction of the pump and probe laser fields, which were reported in transient pump-probe and two-dimensional ultrafast spectroscopy.[65-70] The frequency-dependent anisotropy decay of the IR probe in different polymers is shown in Figures 2d and 5d. The time constants, t_{ir}, and t_{fve} of the PSC probe are respectively 4.8 ± 0.5 and 228.0 ± 1.1 ps for PMMA, 5.3 ± 0.4 and 198.4 ± 0.8 ps for PPEA and 8.6 ± 0.6 and 169.6 ± 1.2 ps in PMEA. Again, we confirm that the first and second anisotropy decay time constants in the case of the PMMA are in quantitative agreement with the previous experimental results.[15] The short-time anisotropy decay due to the internal rotational fluctuation of the -SeCN group in PPEA and PMEA are slower. However, this trend in short time regime (10 ps) anisotropy decay in polymers is completely opposite in the ~200 ps time regime, where the t_{fve} of PPEA and PMEA are smaller than that of PMMA. The t_{fve} component of PMMA is ~15% and 25% slower compared to that of PPEA and PMEA respectively. Such a slow orientational diffusion of the IR probe found in PMMA polymer indicates that the confining angular space is smaller in PMMA than in PPEA or PMEA polymer.

The frequency-dependent order parameters related to the anisotropy decays of the IR probe, summarized in Table S5, show that these parameters can change strongly based on the probe frequency. The S_{inert} reflects the amount of missed anisotropy decay dynamics due to the instantaneous nature of the inertial relaxation process, whereas S_{ir} and S_{fve} are the characteristic order parameters related to the orientational relaxation of the IR probe sampling the short-time internal rotational fluctuation and the long-time WIAC-type diffusion processes, respectively. As the order parameter (S_i) and the corresponding cone half-angle (θ_i) are related

to each other (Eqs. (7) and (15)), a large value of S_i corresponds to a small angular space sampled by the respective anisotropy dynamics of the IR probe. Interestingly, S_{inert} does not change much at different probe frequencies, which suggests that the inertial dynamics of the IR probe is weakly dependent on the polymer property. On the other hand, S_{ir} and S_{fve} both strongly depend on the probe frequency. The S_{ir} and S_{fve} increase with higher probe frequency in all three polymers suggesting that the associated orientational diffusion of a subensemble of PSC molecules with high CN stretch frequencies becomes less sterically hindered. In contrast, those PSC molecules with low CN stretch frequencies are in a restricted and confined environment.

Furthermore, the cumulative order parameters $S_{IR}(= S_{inert} \times S_{ir})$ and $S_{tot}(= S_{inert} \times S_{ir} \times S_{fve})$ are useful quantities accounting for the total orientational diffusion of the PSC probe in respectively ~10 ps and ~ 200 ps timescale. Both S_{IR} and S_{tot} also increase with increasing CN stretch frequency, indicating similar behavior reflected by individual order parameters. The larger $\langle S_{IR} \rangle$ and $\langle S_{fve} \rangle$ values of PSC in PMMA than in PPEA and PMEA (see Table S5) indicate that the corresponding confining spaces in PMMA are smaller than other two polymers.

D.1. Cone half-angle distribution

The orientational relaxation of a vibrational probe in internal rotation or WIAC model occurs in a rigid cone with a half-angle of θ_i, which is the characteristic quantity related to the angular space of a cylindrical volume element. Thus, the extent of confinement experienced by a given probe molecule during its orientational dynamics mainly depends on the size of FVE. Fica-Contreras et al.[14] showed that the cone half-angle is quite sensitive to the local microscopic environment around the probe in a given polymer. Using the relationship between the order parameter (S_i) and cone half-angle (θ_i) (Eq. (7) and (15)) and the experimentally

measured S_{inert}, S_{ir}, and S_{fve}, we could estimate the corresponding cone half-angles, θ_{inert}, θ_{ir}, and θ_{fve}. The total short-time cone half-angle θ_{IR} can be derived from the cumulative order parameters S_{IR} which provide information on the sizes of angular spaces sampled by the probe molecule's orientational diffusion at ~10 ps.

The probe frequency-dependent cone half-angles are shown in Figure 6a (Table S9 of Supplementary Note 9). The cone half-angle θ_{inert} associated with the inertial dynamics of the probe molecule increases from 10.6° at 2122.3 cm^{-1} to 14.6° at 2136.5 cm^{-1} for PMMA, which shows the weak dependence of θ_{inert} on the probe beam frequency. In PPEA, θ_{inert} varies from 8.90° to 17.0° whereas from 12.3° to 15.8° for PMEA with increasing probe beam frequency. The cone half-angle θ_{ir} of PMMA increases from 14.2° at 2122.3 cm^{-1} to 25.9° at 2136.5 cm^{-1}. Interestingly, the rate of increase of θ_{ir} in the high-frequency region becomes larger than that in the low-frequency region, suggesting inherent structural heterogeneity representing different subensemble populations of the IR probe embedded in different FVEs. However, θ_{ir} increases monotonically with respect to the probe frequency for both PPEA and PMEA (Figure S11). Very interestingly, we find that the average $\langle\theta_{ir}\rangle$ values of the three polymers are similar to one another, where the ensemble-averaged cone half-angle is defined as

$$\langle\theta_i\rangle = \frac{\int \theta_i(\omega)\sqrt{|S_{1-2}(\omega)|}\, d\omega}{\int \sqrt{|S_{1-2}(\omega)|}\, d\omega}. \tag{23}$$

where $S_{1-2}(\omega)$ is the excited state absorption spectrum. Note that the absolute magnitude of $S_{1-2}(\omega)$ is approximately proportional to the square of the number of PSC molecules absorbing the IR photon with a frequency of ω if the transition dipole moment of CN stretch mode weakly depends on vibrational frequency. Therefore, $\sqrt{|S_{1-2}(\omega)|}$ is approximately equivalent to the ω-dependent number distribution $N(\omega)$ of IR probe molecules, which justifies the definition of the average in Eq. (23). The ensemble-averaged cone half-angles are

summarized in Table 3. Here, it should be noted that there is a difference of ~5-6° between $\langle\theta_{IR}\rangle$ and $\langle\theta_{fve}\rangle$ at different probe beam frequencies for PMMA in this study as opposed to 1-2° in the previous study.[14] The apparent difference in $\langle\theta_{IR}\rangle$ and $\langle\theta_{fve}\rangle$ may be directly related to the polymer molecular weight, local heating contribution contaminating the 0-1 IR-PP signal of CN, different experimental procedures employed to obtain the IR-PP data, and the procedure of the polymer thin film preparation. However, some level of separation between $\langle\theta_{IR}\rangle$ and $\langle\theta_{fve}\rangle$ seems to be logical according to the newly proposed model (Figure 4) discussed in Section C as $\langle\theta_{IR}\rangle$ and $\langle\theta_{fve}\rangle$ represent different confining space sampled by the long timescale separated rotational anisotropy of the IR probe.

The present experimental observation shows that the average $\langle\theta_{ir}\rangle$ or $\langle\theta_{IR}\rangle$ weakly depends on polymers considered here, suggesting that the angular space allowed for a given IR probe molecule to be orientationally relaxed in < 10 ps does not strongly depend on the chemical nature or length of the sidechain functional group of the polymer. The weak polymer dependence of $\langle\theta_{ir}\rangle$ and $\langle\theta_{IR}\rangle$ corroborates well with the internal rotational fluctuation model discussed in section B. Although the available volume for either the WIAC motion or internal rotational relaxation of the CN group is less dependent on the polarity or local electrostatic (dielectric) environment, the rate of rotational relaxation, which is determined by the associated activation energy barrier, could depend on polymers because the intermolecular interaction of polar PSC or simply CN group with neighboring polar polymer side chains determines the corresponding activation energy and barrier heights. The first rotational diffusive process occurring in less than 10 ps is fast in PMMA, whereas that in PMEA is the slowest among the three polymers. Noting that the PMEA side chain is more polar than those of the other two polymers, the interaction between the PSC molecule or its CN group and the side chains of PMEA makes the activation energy of PSC rotation or the potential energy barrier associated with the internal rotational fluctuation of CN group high. In contrast to the weakly polymer-

dependent $\langle\theta_{IR}\rangle$, we found that the average $\langle\theta_{fve}\rangle$ depends on the chemical nature of the polymer strongly. The ensemble-averaged $\langle\theta_{fve}\rangle$ of PMMA is 28.6°, which is substantially smaller than those of the other two polymers, PPEA (59.3°) and PMEA (63.7°) (Figure 6a and Table 3). This notable difference in the static FVE size of PMMA sampled by the WIAC motion of the IR probe from those of PPEA and PMEA suggests that $\langle\theta_{fve}\rangle$ is very sensitive to the chemical nature of the polymer material and are directly related to the biocompatibility of a given polymer.

D.2. Size and probability distribution of FVEs

In an earlier computational work on the isomerization dynamics of n-butane in the condensed phase, a direct relationship between the conformational population and the cavity distribution around the flexible conformer was deduced.[71] Following this concept, we can imagine that the internal rotational fluctuation of the -SeCN unit should have a direct connection with the FVE around it, whereas the overall molecular rotation experiences the void space sampled by the distant para-hydrogen atom. So, we will try to shed light on these two spatially separated FVEs in a stepwise fashion. We find that the cone half-angles, θ_{IR} and θ_{fve} associated with corresponding FVEs are important parameters reflecting their impact on the orientational relaxation dynamics of the IR probe in polymers. Both θ_{IR} and θ_{fve} show the same increasing trends with the increasing probe frequency for two polymers, which suggests that the IR probe molecules resides in heterogeneous environments.[14] Now, it becomes possible to convert the measured cone half-angle to the radius (r_i) of the confining cone with respect to the center of mass of the PSC molecule as follows,

$$r_i = a\sin(\theta_i) + \Delta r. \tag{24}$$

Here, two different a and Δr values are used for converting θ_{IR} and θ_{fve} to their respective FVE sizes. For the FVE corresponding to the internal rotational fluctuation, a_{IR} is the distance

between the Se and N atoms of the PSC molecule, (~3.02 Å, obtained from the MP2 optimized structure) and Δr_{IR} is the N atom's van der Waal's radius (1.55 Å). Similarly, for the FVE corresponding to the WIAC motion, a_{fve} is the distance of the terminal p-hydrogen atom of the phenyl ring of the PSC molecule from its center of mass (4.31 Å), and Δr_{fve} corresponds to the radius of the p-hydrogen atom (1.2 Å).[72] The FVE radii calculated by using Eq. (24) are summarized in Table S9 at different CN stretch band frequencies.

We next calculated the probability distributions of r_{IR} and r_{fve} reflecting the overall sizes of FVEs associated with the short-time (<10 ps) internal rotational fluctuation and the long-time (~200 ps) WIAC motion, respectively. To understand how different subensemble populations of FVEs are distributed at different probe beam frequencies, the center-weighted probability distribution was calculated by estimating the weight factor from the weighted average of the area normalized signal intensity of the 1-2 pump-probe spectra of the CN stretch band at a particular probe beam frequency as

$$P\{r_j(\omega_i)\} = \frac{\left[\left\{\frac{S_{12}(\omega_i)}{A_{12}}\right\}\Big/\sum_{\omega_i}\left\{\frac{S_{12}(\omega_i)}{A_{12}}\right\}\right] \times r_j(\omega_i)}{\sum_{\omega_i}\left[\left\{\frac{S_{12}(\omega_i)}{A_{12}}\right\}\Big/\sum_{\omega_i}\left\{\frac{S_{12}(\omega_i)}{A_{12}}\right\}\right] \times r_j(\omega_i)}. \quad (25)$$

where $S_{12}(\omega_i)$ is the signal intensity of the 1-2 pump-probe spectrum of the nitrile stretch band at 0.2 ps at different probe beam frequencies, A_{12} is the total area of the 1-2 pump-probe spectrum, $r_j(\omega_i)$ is the calculated FVE radius for that specific probe frequency, and j reflects the type of radius (r_{IR}/r_{fve}) being calculated. Here, the weighted average value of the area normalized intensity (term inside the square bracket) is used to assign higher priority to the probability distribution close to the center frequency of the 1-2 pump-probe spectra as opposed to the edge such that $\sum_{\omega_i}\left\{\frac{S_{12}(\omega_i)}{A_{12}}\Big/\sum_{\omega_i}\frac{S_{12}(\omega_i)}{A_{12}}\right\} = 1$. This is particularly important as the anisotropy decay close to the center frequency has a higher signal-to-noise ratio than the edge. Further, the denominator term is used to obtain the normalized probability distribution of FVEs.

The center-weighted probability distributions of the FVE size $r_{IR}(\omega)$, and $r_{fve}(\omega)$, which are $P\{r_{IR}(\omega)\}$ and $P\{r_{fve}(\omega)\}$ calculated using Eq. (25), are shown in Figures 6b-6c for all the polymers. Both $P\{r_{IR}(\omega)\}$ and $P\{r_{fve}(\omega)\}$ are fitted with the Gaussian function to estimate the center position, which corresponds to the most probable radius (r_i^{mp}) associated with each type of FVE. The relevant fitting parameters, including the center positions and the FWHM's of $P\{r_{IR}(\omega)\}$ and $P\{r_{fve}(\omega)\}$, are summarized in Table S12 of Supplementary Note 11. We found that the estimated r_{IR}^{mp} is 2.73 ± 0.02 Å for PMMA, whereas the r_{IR}^{mp} is estimated to be 2.91 ± 0.02 Å in PPEA and 2.95 ± 0.03 Å in PMEA. This independence of r_{IR}^{mp} on the polymer properties can be understood because it is related to the internal rotational fluctuation of the nitrile mode.

In contrast to the r_{IR}^{mp}, the difference in the r_{fve}^{mp} between these polymers is considerably large. The r_{fve}^{mp} of PMMA, which reflects the average static FVE size is 3.28 ± 0.03 Å. Our estimated r_{fve}^{mp} is larger than those (2.9-3.0 Å) obtained by using time-resolved IR-PP anisotropy measurement and PALS experiment. The apparent difference in FVE sizes may appear from different experimental procedures employed or different probe sizes used. A notable observation here is that the r_{fve}^{mp} is 4.91 ± 0.01 Å in PPEA and 5.10 ± 0.02 Å in PMEA polymer, which is respectively 49% and 55% larger than in PMMA. This substantial increase in the total FVE sizes of PPEA indicates the profound difference in their structural organization at the microscopic level. The ensemble-averaged FVE radii, $\langle r_{IR} \rangle$ and $\langle r_{fve} \rangle$ are also calculated (Table S11), which are in good agreement with the r_{IR}^{mp} and r_{fve}^{mp} obtained from the Gaussian fitting of the FVE size probability distribution. Further, the impact of these changes is crucial to understanding their macroscopic behavior and material properties.

3. Correlation of the FVE size and probability distribution with individual biocompatible behavior

The FVE size and probability distribution of the amorphous PMMA, PPEA, and PMEA polymer determined from the anisotropy relaxation dynamics of the CN stretch band of PSC entrapped inside FVEs, report exciting results. The estimated static FVE radius, r_{fve}^{mp} is the most appropriate parameter for directly comparing the FVE size at different polymers. The r_{fve}^{mp} in PPEA and PMEA, increases substantially than in PMMA polymer. On the other hand, the gas and solvent permeability in the amorphous polymer material was previously assigned to the large FVEs.[7, 11, 57-59] Hence, we anticipate that this larger size FVE in PPEA and PMEA is suitable for higher water permeability compared to PMMA polymer. This higher water permeability in PPEA and PMEA may facilitate stronger water interaction with the respective polymer matrix than in PMMA polymer, as observed in our previous study.[56] Furthermore, the larger sidechain functional group in both PPEA (-OCH_2CH_2OPh) and PMEA (-OCH_2CH_2OMe) polymers compared to that in PMMA (-OCH_3) may have a crucial role to play in dictating their corresponding FVE sizes. However, this relationship may not be straightforward as -OCH_2CH_2OPh in the PPEA sidechain is bulkier than -OCH_2CH_2OMe in PMEA. Therefore, we anticipate that both the chemical nature of the sidechain functional group as well as their local interactions at the microscopic level play a pivotal role that could impact the FVE size and probability distribution making the PMEA polymer matrix highly favorable for its strong interaction with water as compared to PPEA.[56] Ironically, PMEA is significantly more biocompatible than PPEA polymer. Therefore, it may imply that the larger FVE size in tandem with comparatively higher flexibility in its structural organization and local interactions at the microscopic level may be the origin of the strong biocompatible behavior of PMEA.

Further, a smaller FVE radius and smaller sidechain functional group of the PMMA polymer matrix result in restricted water permeability, which could help understand its strong

hydrophobic character. Furthermore, it could be predicted that PMMA would have more mechanical strength and slow physical aging than those in PPEA and PMEA polymers due to the smaller FVE sizes. Therefore, this study elucidates detailed intricacies of the FVE sizes and local interactions among sidechain functional groups of the amorphous polymer material and their role in dictating their macroscopic behavior, including biocompatibility and hydrophobicity. We shall present our experimental and simulation results on the variation of FVEs in different biocompatible polymers elsewhere.

3. Summary and a few concluding remarks

In summary, the present work unravels the role of the internal rotational fluctuation of the IR probe on the molecular anisotropy decay by comparing three IR probes in the acrylate-based amorphous polymers by utilizing the polarization-selective IR-PP spectroscopy and MD simulation techniques. The study reveals significant variations in the constrained orientational relaxation dynamics of the CN stretch mode of PSC than in MPSC and DMPSC in PMMA. The study demonstrates that the short-time anisotropy decay of the CN stretch mode (occurring in <10 ps) primarily originates from the internal rotational fluctuation of the -SeCN moiety along the C(Ph)-Se bond vector. Interestingly, the angular space explored by the internal rotational fluctuation of the probes (r_{IR}^{mp}) does not exhibit substantial variation among different polymers, aligning well with the internal rotation model. We discuss the theoretical foundation of various molecular processes associated with the time-separated rotational anisotropy of the IR probe in detail. Furthermore, MD simulations indicate the absence of segmental motion within the experimental observation window, suggesting that the actual size of the FVEs is probed only through the long-time anisotropy decay of the IR probe. The current findings highlight that the r_{fve}^{mp}, representing the size of the FVEs, strongly depends on the polymer properties and notably increases from PMMA to PMEA polymer and can be adequately tuned for specific needs. The larger FVE size in PMEA polymer, in conjunction with the chemical

nature of its bulky sidechain functional group and the local interactions within the polymer matrix, elucidates the stronger water interaction leading to higher water permeation observed in PMEA. This insight provides a potential explanation for the excellent biocompatible characteristics exhibited by PMEA. Conversely, the smaller r_{fve}^{mp} in PMMA polymer helps account for its strong hydrophobic nature. This detailed understanding offers a potential explanation for how the rotational relaxation of an IR probe at different time scales samples distinct FVEs, providing valuable insights into their relationship.

Nonetheless, in our opinion, a drawback of the current method with an IR probe whose size is still larger than typical void spaces in polymers is that the FVE sampling by the rotational anisotropy is constrained by the size of the probe itself, thereby preventing the acquisition of information on FVEs smaller than the probe size. As a result, the obtained FVE size and distribution may deviate to some extent from the actual FVE properties, indicating that the current method also depends on the properties of the specific probe used. In order to address this limitation, it may be beneficial to combine the results obtained from multiple IR probes with different molecular sizes for the FVE analysis, which could provide insights closer to the actual FVE properties. In conclusion, this study sheds light on crucial factors and intricate aspects of the structural organization of polymer matrices, which contribute to the accurate estimation of FVEs using ultrafast infrared spectroscopy with an IR probe with a long vibrational lifetime.

ASSOCIATED CONTENT

Supporting Information. The supporting information is available free of charge on the ACS Publication website at DOI:
Experimental details, sample preparation, fitting of the FT-IR spectra of the nitrile band of various IR probes in polymers, the IR-PP signal of the 0-1 and 1-2 transition of the nitrile probe, denoising procedure of the IR-PP signal of the CN stretch mode using the one-dimensional deconvolution algorithm based on the discrete wavelet transform (DWT) analyses, isotropic IR-PP signal and global fitting analysis of the anisotropic IR-PP signal of the nitrile mode, probe-beam frequency dependent order parameters, methodology and simulation details,

probe-beam frequency-dependent cone half-angle distribution of the CN stretch mode, FVE sizes and distribution and corresponding Gaussian fitting.

AUTHOR INFORMATION

ORCID
Saptarsi Mondal: 0000-0003-1140-9322
Kyungwon Kwak: 0000-0003-1680-0996
Minhaeng Cho: 0000-0003-1618-1056

Notes
The author declares no competing financial interest.

ACKNOWLEDGMENTS

This work was supported by the Institute for Basic Science (IBS-R023-D1) (MC) and a National Research Foundation of Korea (NRF) grant funded by the Korean government (MSIT)(NRF-2020R1A2C2010675 and NRF-2020R1A5A1019141) (KK).

4. References

(1) Yang, J.; Tao, L.; He, J.; McCutcheon, J. R.; Li, Y. Machine learning enables interpretable discovery of innovative polymers for gas separation membranes. *Science Adv.* **2022**, *8* (29), eabn9545.
(2) Park, H. B.; Jung, C. H.; Lee, Y. M.; Hill, A. J.; Pas, S. J.; Mudie, S. T.; Van Wagner, E.; Freeman, B. D.; Cookson, D. J. Polymers with Cavities Tuned for Fast Selective Transport of Small Molecules and Ions. *Science* **2007**, *318* (5848), 254-258.
(3) Budd, P. M.; McKeown, N. B.; Fritsch, D. Free volume and intrinsic microporosity in polymers. *J. Mater. Chem.* **2005**, *15* (20), 1977-1986, 10.1039/B417402J.
(4) Patterson, D. Free Volume and Polymer Solubility. A Qualitative View. *Macromolecules* **1969**, *2* (6), 672-677.
(5) Low, Z.-X.; Budd, P. M.; McKeown, N. B.; Patterson, D. A. Gas Permeation Properties, Physical Aging, and Its Mitigation in High Free Volume Glassy Polymers. *Chem. Rev.* **2018**, *118* (12), 5871-5911.
(6) O'Connor, K. M.; Scholsky, K. M. Free volume effects on the melt viscosity of low molecular weight poly(methyl methacrylate). *Polymer* **1989**, *30* (3), 461-466.
(7) Coll, H.; Searles, C. G. Solvent permeation rates and ageing phenomena in polymer coatings. *Polymer* **1988**, *29* (7), 1266-1272.
(8) Greiner, R.; Schwarzl, F. R. Thermal contraction and volume relaxation of amorphous polymers. *Rheol. Acta* **1984**, *23* (4), 378-395.
(9) Chow, T. S. Kinetics of free volume and physical aging in polymer glasses. *Macromolecules* **1984**, *17* (11), 2336-2340.
(10) Knauss, W. G.; Emri, I. J. Non-linear viscoelasticity based on free volume consideration. *Comput. Struct.* **1981**, *13* (1), 123-128.
(11) Peterson, C. M. Permeability studies on heterogeneous polymer films. *J. Appl. Polym. Sci.* **1968**, *12* (12), 2649-2667.
(12) Cohen, M. H.; Turnbull, D. Molecular Transport in Liquids and Glasses. *J. Chem. Phys.* **1959**, *31* (5), 1164-1169.
(13) White, R. P.; Lipson, J. E. G. Polymer Free Volume and Its Connection to the Glass Transition. *Macromolecules* **2016**, *49* (11), 3987-4007.

(14) Fica-Contreras, S. M.; Hoffman, D. J.; Pan, J.; Liang, C.; Fayer, M. D. Free Volume Element Sizes and Dynamics in Polystyrene and Poly(methyl methacrylate) Measured with Ultrafast Infrared Spectroscopy. *J. Am. Chem. Soc.* **2021**, *143* (9), 3583-3594.
(15) Hoffman, D. J.; Fica-Contreras, S. M.; Fayer, M. D. Amorphous polymer dynamics and free volume element size distributions from ultrafast IR spectroscopy. *Proc. Natl. Acad. Sci. U.S.A.* **2020**, *117* (25), 13949-13958.
(16) Kinosita, K., Jr.; Kawato, S.; Ikegami, A. A theory of fluorescence polarization decay in membranes. *Biophys. J.* **1977**, *20* (3), 289-305. From NLM.
(17) Jansen, J. C.; Macchione, M.; Tocci, E.; De Lorenzo, L.; Yampolskii, Y. P.; Sanfirova, O.; Shantarovich, V. P.; Heuchel, M.; Hofmann, D.; Drioli, E. Comparative Study of Different Probing Techniques for the Analysis of the Free Volume Distribution in Amorphous Glassy Perfluoropolymers. *Macromolecules* **2009**, *42* (19), 7589-7604.
(18) Yampolskii, Y. P. Methods for investigation of the free volume in polymers. *Russ. Chem. Rev.* **2007**, *76* (1), 59-78.
(19) Félix, M. V.; Consolati, G.; Velázquez, R.; Castaño, V. M. Positron annihilation studies of nanoholes and microphase formation control of a PMMA+MMA+TEGDMA system. *Polymer* **2006**, *47* (1), 265-271.
(20) Zheng, J.; Kwak, K.; Asbury, J.; Chen, X.; Piletic, I. R.; Fayer, M. D. Ultrafast Dynamics of Solute-Solvent Complexation Observed at Thermal Equilibrium in Real Time. *Science* **2005**, *309* (5739), 1338-1343.
(21) Park, S.; Shin, J.; Yoon, H.; Lim, M. Rotational Isomerization of Carbon–Carbon Single Bonds in Ethyl Radical Derivatives in a Room-Temperature Solution. *J. Phys. Chem. Lett.* **2022**, *13* (49), 11551-11557.
(22) Ishihara, K. Blood-Compatible Surfaces with Phosphorylcholine-Based Polymers for Cardiovascular Medical Devices. *Langmuir* **2019**, *35* (5), 1778-1787.
(23) Blackman, L. D.; Gunatillake, P. A.; Cass, P.; Locock, K. E. S. An introduction to zwitterionic polymer behavior and applications in solution and at surfaces. *Chem. Soc. Rev.* **2019**, *48* (3), 757-770, 10.1039/C8CS00508G.
(24) Kobayashi, S.; Wakui, M.; Iwata, Y.; Tanaka, M. Poly(ω-methoxyalkyl acrylate)s: Nonthrombogenic Polymer Family with Tunable Protein Adsorption. *Biomacromolecules* **2017**, *18* (12), 4214-4223.
(25) Hu, G.; Emrick, T. Functional Choline Phosphate Polymers. *J. Am. Chem. Soc* **2016**, *138* (6), 1828-1831.
(26) Hao, H.; Shao, J.; Deng, Y.; He, S.; Luo, F.; Wu, Y.; Li, J.; Tan, H.; Li, J.; Fu, Q. Synthesis and characterization of biodegradable lysine-based waterborne polyurethane for soft tissue engineering applications. *Biomaterials Science* **2016**, *4* (11), 1682-1690, 10.1039/C6BM00588H.
(27) Lin, X.; Fukazawa, K.; Ishihara, K. Photoreactive Polymers Bearing a Zwitterionic Phosphorylcholine Group for Surface Modification of Biomaterials. *ACS Appl. Mater. Interfaces* **2015**, *7* (31), 17489-17498.
(28) Ko, D. Y.; Patel, M.; Jung, B. K.; Park, J. H.; Jeong, B. Phosphorylcholine-Based Zwitterionic Biocompatible Thermogel. *Biomacromolecules* **2015**, *16* (12), 3853-3862.
(29) Kitakami, E.; Aoki, M.; Sato, C.; Ishihata, H.; Tanaka, M. Adhesion and Proliferation of Human Periodontal Ligament Cells on Poly(2-methoxyethyl acrylate) %J BioMed Research International. *Biomed Res. Int.* **2014**, *2014*, 14.
(30) Tada, S.; Inaba, C.; Mizukami, K.; Fujishita, S.; Gemmei-Ide, M.; Kitano, H.; Mochizuki, A.; Tanaka, M.; Matsunaga, T. Anti-Biofouling Properties of Polymers with a Carboxybetaine Moiety. *Macromol. Biosci* **2009**, *9* (1), 63-70.
(31) Yoshikawa, C.; Goto, A.; Tsujii, Y.; Fukuda, T.; Kimura, T.; Yamamoto, K.; Kishida, A. Protein Repellency of Well-Defined, Concentrated Poly(2-hydroxyethyl methacrylate) Brushes by the Size-Exclusion Effect. *Macromolecules* **2006**, *39* (6), 2284-2290.
(32) Yoshizaki, T.; Tabuchi, N.; Van Oeveren, W.; Shibamiya, A.; Koyama, T.; Sunamori, M. PMEA Polymer-Coated PVC Tubing Maintains Anti-Thrombogenic Properties during in vitro Whole Blood Circulation. *Int. J. Artif. Organs* **2005**, *28* (8), 834-840.
(33) Lin, W.-C.; Yu, D.-G.; Yang, M.-C. Blood compatibility of thermoplastic polyurethane membrane immobilized with water-soluble chitosan/dextran sulfate. *Colloids Surf. B* **2005**, *44* (2), 82-92.

(34) Iwasaki, Y.; Ishihara, K. Phosphorylcholine-containing polymers for biomedical applications. *Anal. Bioanal. Chem* **2005**, *381* (3), 534-546.
(35) Kanekura, T.; Nagata, Y.; Miyoshi, H.; Ishihara, K.; Nakabayashi, N.; Kanzaki, T. Beneficial effects of synthetic phospholipid polymer, poly(2-methacryloyloxyethyl phosphorylcholine-co-n-butyl methacrylate), on stratum corneum function. *Clin. Exp. Dermatol.* **2002**, *27* (3), 230-234.
(36) Li, G.; Ye, S.; Morita, S.; Nishida, T.; Osawa, M. Hydrogen Bonding on the Surface of Poly(2-methoxyethyl acrylate). *J. Am. Chem. Soc* **2004**, *126* (39), 12198-12199.
(37) Ye, S.; Morita, S.; Li, G.; Noda, H.; Tanaka, M.; Uosaki, K.; Osawa, M. Structural Changes in Poly(2-methoxyethyl acrylate) Thin Films Induced by Absorption of Bisphenol A. An Infrared and Sum Frequency Generation (SFG) Study. *Macromolecules* **2003**, *36* (15), 5694-5703.
(38) Kitano, H.; Imai, M.; Mori, T.; Gemmei-Ide, M.; Yokoyama, Y.; Ishihara, K. Structure of Water in the Vicinity of Phospholipid Analogue Copolymers As Studied by Vibrational Spectroscopy. *Langmuir* **2003**, *19* (24), 10260-10266.
(39) Tanaka, M.; Mochizuki, A.; Shiroya, T.; Motomura, T.; Shimura, K.; Onishi, M.; Okahata, Y. Study on kinetics of early stage protein adsorption on poly(2-methoxyethylacrylate) (PMEA) surface. *Colloids Surf. A* **2002**, *203* (1), 195-204.
(40) Tanaka, M.; Mochizuki, A.; Ishii, N.; Motomura, T.; Hatakeyama, T. Study of Blood Compatibility with Poly(2-methoxyethyl acrylate). Relationship between Water Structure and Platelet Compatibility in Poly(2-methoxyethylacrylate-co-2-hydroxyethylmethacrylate). *Biomacromolecules* **2002**, *3* (1), 36-41.
(41) Tanaka, M.; Motomura, T.; Kawada, M.; Anzai, T.; Yuu, K.; Shiroya, T.; Shimura, K.; Onishi, M.; Akira, M. Blood compatible aspects of poly(2-methoxyethylacrylate) (PMEA)—relationship between protein adsorption and platelet adhesion on PMEA surface. *Biomaterials* **2000**, *21* (14), 1471-1481.
(42) Sato, K.; Kobayashi, S.; Kusakari, M.; Watahiki, S.; Oikawa, M.; Hoshiba, T.; Tanaka, M. The Relationship Between Water Structure and Blood Compatibility in Poly(2-methoxyethyl Acrylate) (PMEA) Analogues. *Macromol. Biosci.* **2015**, *15* (9), 1296-1303.
(43) Hatakeyama, T.; Tanaka, M.; Hatakeyama, H. Studies on bound water restrained by poly(2-methacryloyloxyethyl phosphorylcholine): Comparison with polysaccharide–water systems. *Acta Biomaterialia* **2010**, *6* (6), 2077-2082.
(44) Myalitsin, A.; Ghosh, S.; Urashima, S.-h.; Nihonyanagi, S.; Yamaguchi, S.; Aoki, T.; Tahara, T. Structure of Water and Polymer at the Buried Polymer/Water Interface Unveiled by Heterodyne-Detected Vibrational Sum Frequency Generation. *Phys. Chem. Chem. Phys.* **2020**, 10.1039/D0CP02618B.
(45) Zhang, F.; Wang, R.; He, Y.; Lin, W.; Li, Y.; Shao, Y.; Li, J.; Ding, M.; Luo, F.; Tan, H.; et al. A biomimetic hierarchical structure with a hydrophilic surface and a hydrophobic subsurface constructed from waterborne polyurethanes containing a self-assembling peptide extender. *J. Mater. Chem. B* **2018**, *6* (26), 4326-4337, 10.1039/C8TB01279B.
(46) Hoshiba, T.; Yoshihiro, A.; Tanaka, M. Evaluation of initial cell adhesion on poly (2-methoxyethyl acrylate) (PMEA) analogous polymers. *J. Biomater. Sci.* **2017**, *28* (10-12), 986-999.
(47) Hirata, T.; Matsuno, H.; Kawaguchi, D.; Inutsuka, M.; Hirai, T.; Tanaka, M.; Tanaka, K. Dynamics of a bioinert polymer in hydrated states by dielectric relaxation spectroscopy. *Phys. Chem. Chem. Phys.* **2017**, *19* (2), 1389-1394, 10.1039/C6CP07322K.
(48) Bag, M. A.; Valenzuela, L. M. Impact of the Hydration States of Polymers on Their Hemocompatibility for Medical Applications: A Review. *Int. J. Mol. Sci* **2017**, *18* (8), 1422.PMC.
(49) Swift, T.; Swanson, L.; Geoghegan, M.; Rimmer, S. The pH-responsive behaviour of poly(acrylic acid) in aqueous solution is dependent on molar mass. *Soft Matter* **2016**, *12* (9), 2542-2549, 10.1039/C5SM02693H.
(50) Kashid, S. M.; Jin, G. Y.; Bagchi, S.; Kim, Y. S. Cosolvent Effects on Solute–Solvent Hydrogen-Bond Dynamics: Ultrafast 2D IR Investigations. *J. Phys. Chem. B* **2015**, *119* (49), 15334-15343.
(51) Hoshiba, T.; Nemoto, E.; Sato, K.; Orui, T.; Otaki, T.; Yoshihiro, A.; Tanaka, M. Regulation of the Contribution of Integrin to Cell Attachment on Poly(2-Methoxyethyl Acrylate) (PMEA) Analogous Polymers for Attachment-Based Cell Enrichment. *PLOS ONE* **2015**, *10* (8), e0136066.
(52) Fukushima, K.; Tsai, M.-Y.; Ota, T.; Haga, Y.; Matsuzaki, K.; Inoue, Y.; Tanaka, M. Evaluation of the hemocompatibility of hydrated biodegradable aliphatic carbonyl polymers with a subtle

difference in the backbone structure based on the intermediate water concept and surface hydration. *Polym. J.* **2015**, *47*, 469, Rapid Communication.
(53) Morita, S.; Tanaka, M. Effect of Sodium Chloride on Hydration Structures of PMEA and P(MPC-r-BMA). *Langmuir* **2014**, *30* (35), 10698-10703.
(54) Tanaka, M.; Hayashi, T.; Morita, S. The roles of water molecules at the biointerface of medical polymers. *Polym. J.* **2013**, *45*, 701, Invited Review.
(55) Morita, S.; Tanaka, M.; Kitagawa, K.; Ozaki, Y. Hydration Structure of Poly(2-methoxyethyl acrylate): Comparison with a 2-Methoxyethyl Acetate Model Monomer. *J. Biomater. Sci.* **2010**, *21* (14), 1925-1935.
(56) Mondal, S.; Kang, J.; Park, K.; Lim, J. M.; Ha, J.-H.; Kwak, K.; Cho, M. Adsorbed Water Structure on Acrylate-Based Biocompatible Polymer Surface. *J. Phys. Chem. Lett.* **2021**, *12* (38), 9275-9282.
(57) Shieh, Y.-T.; Liu, K.-H. Solubility of CO2 in Glassy PMMA and PS over a Wide Pressure Range: The Effect of Carbonyl Groups. *J. Polym. Res.* **2002**, *9* (2), 107-113.
(58) Poulsen, L.; Ogilby, P. R. Oxygen Diffusion in Glassy Polymer Films: Effects of Other Gases and Changes in Pressure. *J. Phys. Chem. A* **2000**, *104* (12), 2573-2580.
(59) Charlesworth, J. M.; Gan, T. H. Kinetics of Quenching of Ketone Phosphorescence by Oxygen in a Glassy Matrix. *J. Phys. Chem.* **1996**, *100* (36), 14922-14927.
(60) Park, K.-H.; Jeon, J.; Park, Y.; Lee, S.; Kwon, H.-J.; Joo, C.; Park, S.; Han, H.; Cho, M. Infrared Probes Based on Nitrile-Derivatized Prolines: Thermal Insulation Effect and Enhanced Dynamic Range. *J. Phys. Chem. Lett.* **2013**, *4* (13), 2105-2110.
(61) Frisch, M. J.; Trucks, G. W.; Schlegel, H. B.; Scuseria, G. E.; Robb, M. A.; Cheeseman, J. R.; Scalmani, G.; Barone, V.; Petersson, G. A.; Nakatsuji, H.; et al. Gaussian 16 Rev. B.01. Wallingford, CT, 2016.
(62) Marenich, A. V.; Cramer, C. J.; Truhlar, D. G. Universal Solvation Model Based on Solute Electron Density and on a Continuum Model of the Solvent Defined by the Bulk Dielectric Constant and Atomic Surface Tensions. *J. Phys. Chem. B* **2009**, *113* (18), 6378-6396.
(63) Lipari, G.; Szabo, A. Effect of librational motion on fluorescence depolarization and nuclear magnetic resonance relaxation in macromolecules and membranes. *Biophys. J.* **1980**, *30* (3), 489-506.
(64) Jo, S.; Kim, T.; Iyer, V. G.; Im, W. CHARMM-GUI: A web-based graphical user interface for CHARMM. *J. Comput. Chem.* **2008**, *29* (11), 1859-1865.
(65) Brosseau, P.; Seiler, H.; Palato, S.; Sonnichsen, C.; Baker, H.; Socie, E.; Strandell, D.; Kambhampati, P. Perturbed free induction decay obscures early time dynamics in two-dimensional electronic spectroscopy: The case of semiconductor nanocrystals. *J. Chem. Phys.* **2023**, *158* (8).
(66) Dietzek, B.; Pascher, T.; Sundström, V.; Yartsev, A. Appearance of coherent artifact signals in femtosecond transient absorption spectroscopy in dependence on detector design. *Laser Phys. Lett.* **2007**, *4* (1), 38.
(67) Lebedev, M. V.; Misochko, O. V.; Dekorsy, T.; Georgiev, N. On the nature of "coherent artifact". *J. Exp. Theor. Phys.* **2005**, *100* (2), 272-282.
(68) Ferwerda, H. A.; Terpstra, J.; Wiersma, D. A. Discussion of a ''coherent artifact'' in four-wave mixing experiments. *J. Chem. Phys.* **1989**, *91* (6), 3296-3305.
(69) Engh, R. A.; Petrich, J. W.; Fleming, G. R. Removal of coherent coupling artifact in ground-state recovery experiments: malachite green in water-methanol mixtures. *J. Phys. Chem.* **1985**, *89* (4), 618-621.
(70) Balk, M. W.; Fleming, G. R. Dependence of the coherence spike on the material dephasing time in pump–probe experiments. *J. Chem. Phys.* **1985**, *83* (9), 4300-4307.
(71) Chandler, D. Statistical mechanics of isomerization dynamics in liquids and the transition state approximation. *J. Chem. Phys.* **2008**, *68* (6), 2959-2970.
(72) Zhao, Y. H.; Abraham, M. H.; Zissimos, A. M. Fast Calculation of van der Waals Volume as a Sum of Atomic and Bond Contributions and Its Application to Drug Compounds. *J. Org. Chem.* **2003**, *68* (19), 7368-7373.

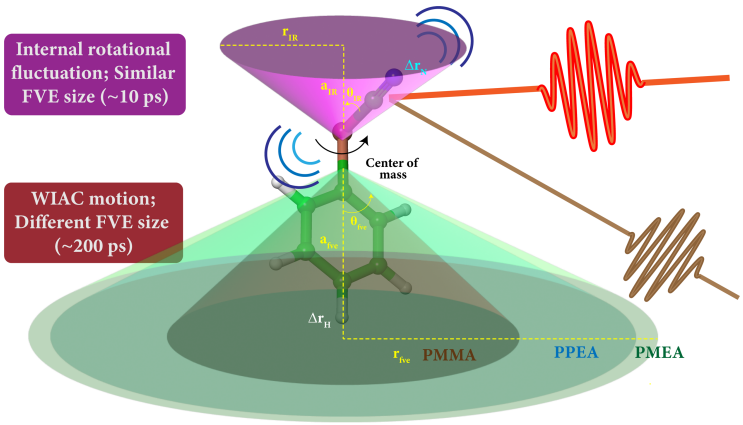

For Table of Contents Only

Table 1. Time constants ($\langle t_1 \rangle$, $\langle t_2 \rangle$ in ps) of frequency-dependent anisotropy decay $[r(t)]$ obtained from global fitting analysis using biexponential function with a constant offset, whereas time constant ($\langle T \rangle$ in ps) of corresponding isotropic relaxation dynamics $[P_{iso}(t)]$ using a single exponential function of the CN stretch mode of PSC in PMMA and PPEA along with MPSC and DMPSC in PMMA. The detailed fitting parameters at different probe beam frequencies can be found in Table S4 and Table S5 of the Supplementary Material.

IR probe	$\langle t_1 \rangle$ (ps)	$\langle t_2 \rangle$ (ps)	$\langle T \rangle$ (ps)
PSC in PMMA	4.8 ± 0.5	228.0 ± 1.1	423.3 ± 0.6
MPSC in PMMA	28.7 ± 1.4	246.9 ± 8.8	587.1 ± 1.9
DMPSC in PMMA	31.9 ± 1.8	284.5 ± 11.5	553.8 ± 2.4
PSC in PPEA	5.3 ± 0.5	198.4 ± 0.8	340.6 ± 0.5
PSC in PMEA	8.6 ± 0.6	169.6 ± 1.2	379.1 ± 0.5

Table 2. Fit parameters of simulated $C_2(t)$ depicted in Figure 3a using Eq. (4). The times constants of the inertial dynamics, a_2, and τ_1 values obtained by fitting simulated $C_2(t)$ from frozen ring approximation with Eq. (20) are presented in parentheses (see Table S6).

IR probe	a_1	$\delta(t)$ (ps)	a_2	τ_1 (ps)	a_3	τ_2 (ps)	a_4
PSC	0.223	0.30 (0.20)	0.078 (0.05)	7.85 (9.68)	0.0873	202.5	0.612
MPSC	0.305	0.35 (0.20)	0.028 (0.02)	24.67 (22.74)	0.076	331.0	0.590
DMPSC	0.223	0.44 (0.20)	0.019 (0.02)	27.71 (24.52)	0.058	606.6	0.699
Mimic DMPSC	0.194	0.47	0.031	15.01	0.143	380.2	0.633

Table 3. Ensemble-averaged cone half-angle sampled by the inertial relaxation ($\langle\theta_{inert}\rangle$), internal rotation ($\langle\theta_{ir}\rangle$), the total cone half-angle $\langle\theta_{IR}\rangle$, and WIAC motion occurring at respectively ~ 10 ps and ~200 ps timescale for PMMA and PPEA polymer matrices. The standard error of the mean in estimating $\langle\theta_i\rangle$ remains ≤ ± 0.5°.

System	$\langle\theta_{Inert}\rangle$ (°)	$\langle\theta_{ir}\rangle$ (°)	$\langle\theta_{fve}\rangle$ (°)	$\langle\theta_{IR}\rangle$ (°)
PMMA	12.8	18.0	28.6	22.1
PPEA	13.2	23.2	59.3	26.6
PMEA	14.0	22.6	63.7	26.5

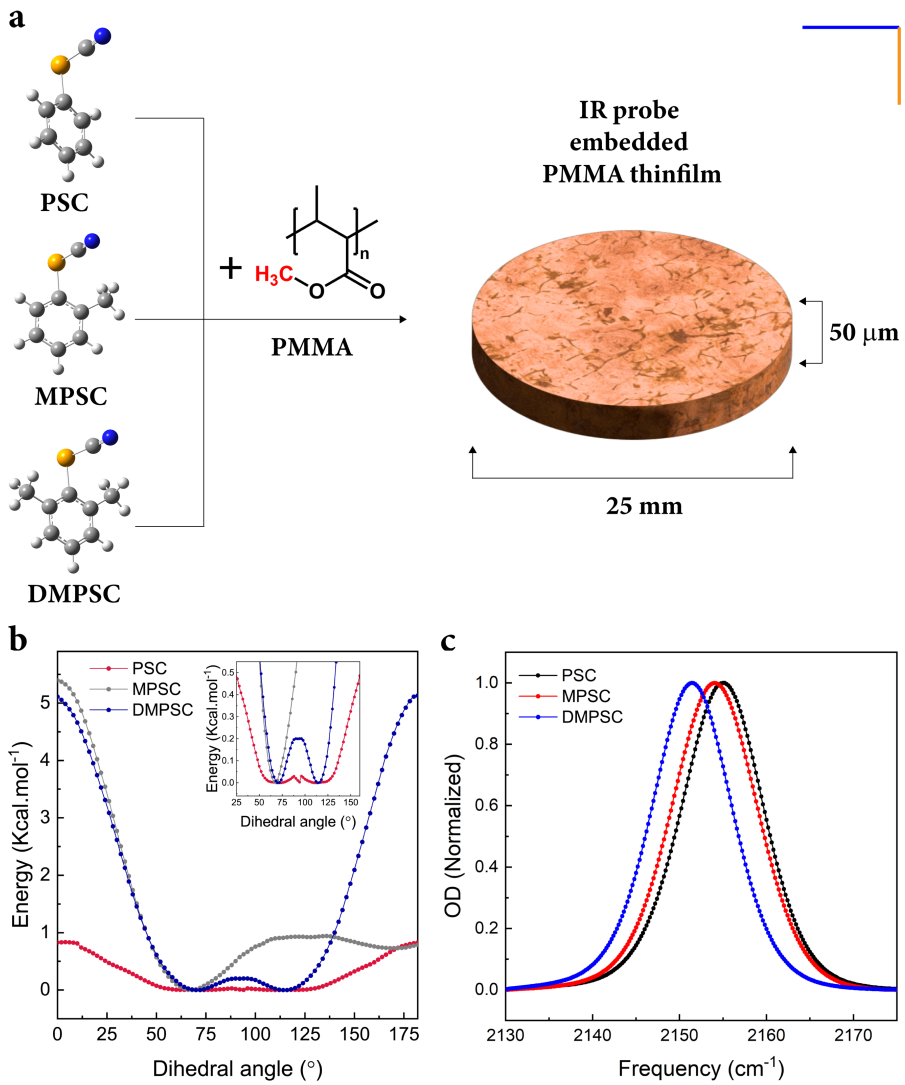

Figure 1. (a) PSC, MPSC and DMPSC embedded polymer thin-film of PMMA. (b) Relaxed Potential energy surface (PES) scan for C(Ph)-C(Ph)-Se-CN dihedral rotation calculated at MP2/6-311+G(D) level of theory using SMD solvation model for the polymer environment. (c) Background subtracted and normalized FT-IR spectra PSC (black), MPSC (red), and DMPSC (blue) IR probe embedded in PMMA thin film. The points represent the experimental data at different frequencies, whereas the solid curves represent the fitting line using the Voigt function.

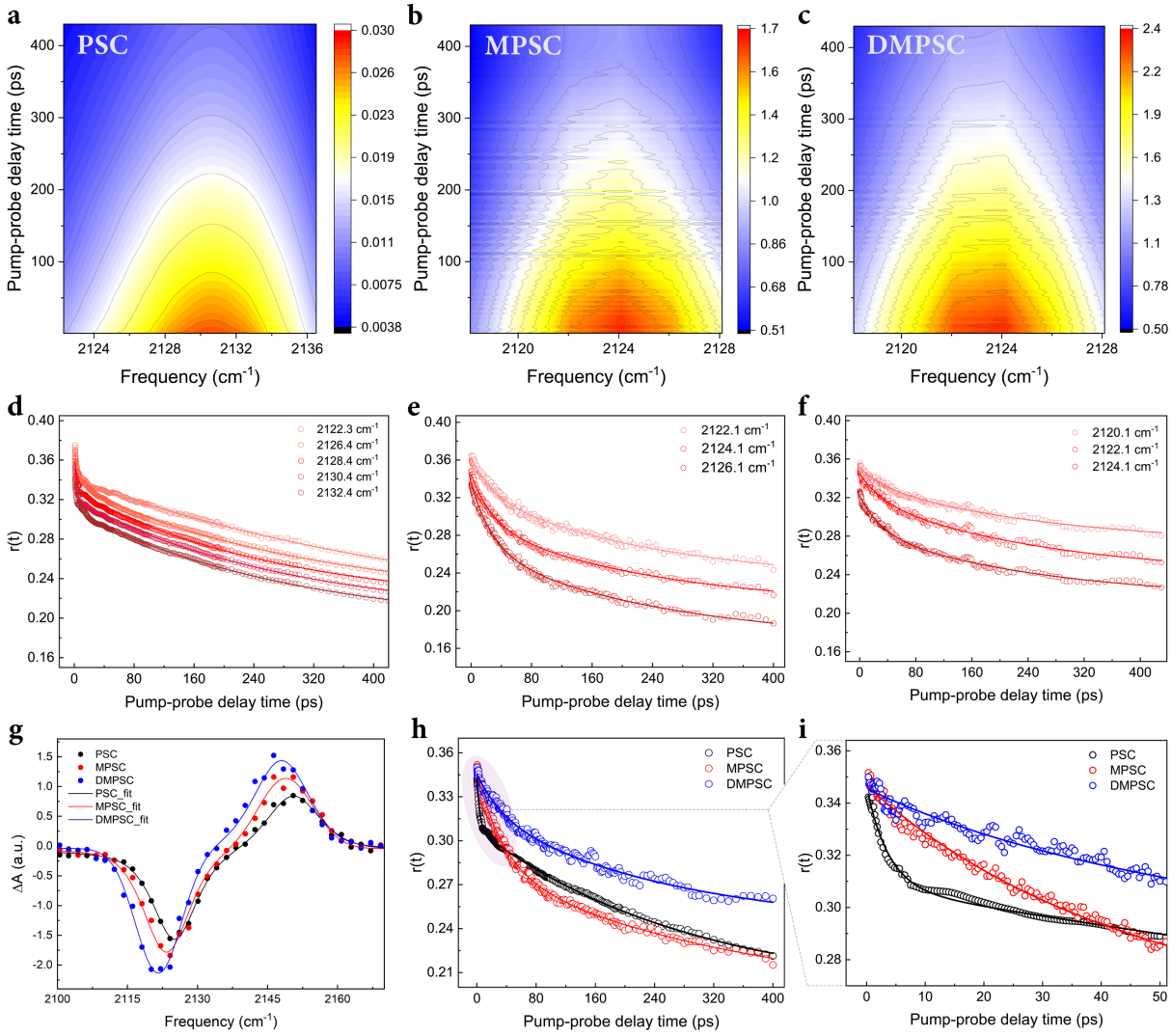

Figure 2. The contour plot of the DWT-corrected 1-2 IR-PP spectra of the CN stretch mode of the (a) PSC, (b) MPSC and (c) DMPSC IR probe embedded in the void spaces of PMMA. The raw 0-1 and 1-2 pump-probe spectra are presented in Supplementary Notes 5 and 6, showing that the DWT correction significantly improves the signal-to-noise ratio of the 1-2 band. Further, probe beam frequency-dependent orientational relaxation dynamics $[r(t)]$ for the 1-2 transition and corresponding global fitting curves (solid lines) using bi-exponential fitting with a constant offset for (d) PSC, (e) MPSC and (f) DMPSC in PMMA polymer matrix; (g) comparison of the 1-2 pump-probe spectra of the -SeCN stretch band of PSC (black), MPSC (red), and DMPSC (blue) in PMMA and (h) their corresponding anisotropy decay at the center frequency of the 1-2 band whereas (i) comparison of the anisotropy decay for the 1-2 transition of the nitrile stretch mode within 50 ps showing that how orientational relaxation dynamics of the nitrile stretch mode of MPSC and DMPSC are substantially slower than that in PSC in PMMA within short-time regime.

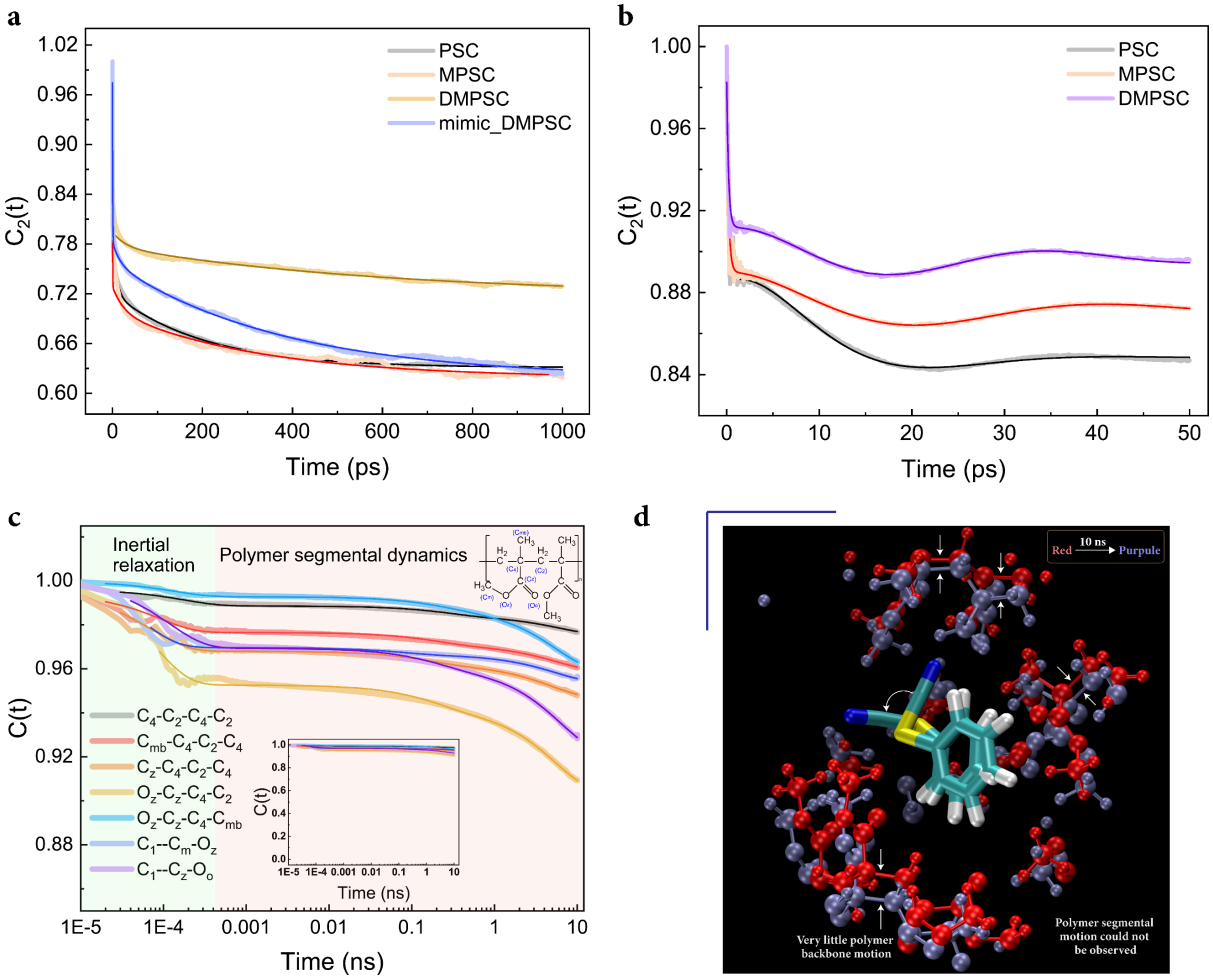

Figure 3. (a) Simulated rotational anisotropy of CN bond vector of PSC (grey), MPSC (red), DMPSC (blue) and mimic DMPSC (violet) in PMMA polymer along with their corresponding fit lines using Eq. 5, (b) simulated rotational anisotropy of CN bond vector of PSC, MPSC, DMPSC in which phenyl ring atoms are kept frozen, (c) TCFs of fluctuations in different dihedral angles and reorinational motions of sidechain bond vectors in PMMA polymer, and (d) snapshot of initial polymer configuration (0 fs, polymer is represented in red) around 6Å from the center of mass of PSC molecule is superimposed to the snapshot of final simulated configuration (10 ns, purple). The polymer backbone remains little altered after 10 ns simulation showing that the polymer segmental motion is insignificant within this time regime.

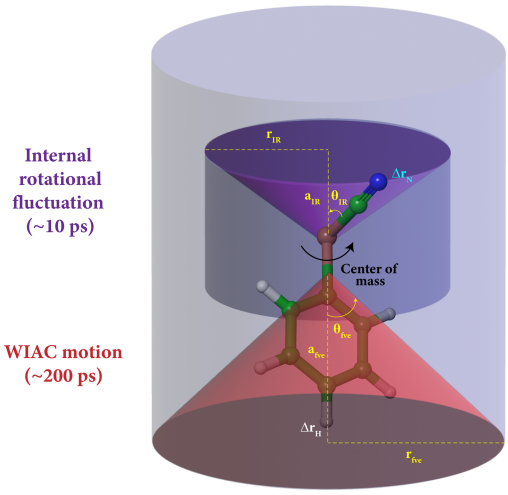

Figure 4. The proposed model where the anisotropy dynamics of the vibrational probe PSC samples the cone half-angle (presented in violet) through the internal rotational fluctuation of the -SeCN moiety about the C(Ph)-Se(CN) bond vector at ~10 ps timescale indicated in violet, whereas in the longer timescale of ~200 ps, it probes the bigger cone semiangle indicated by dark red through the WIAC motion.

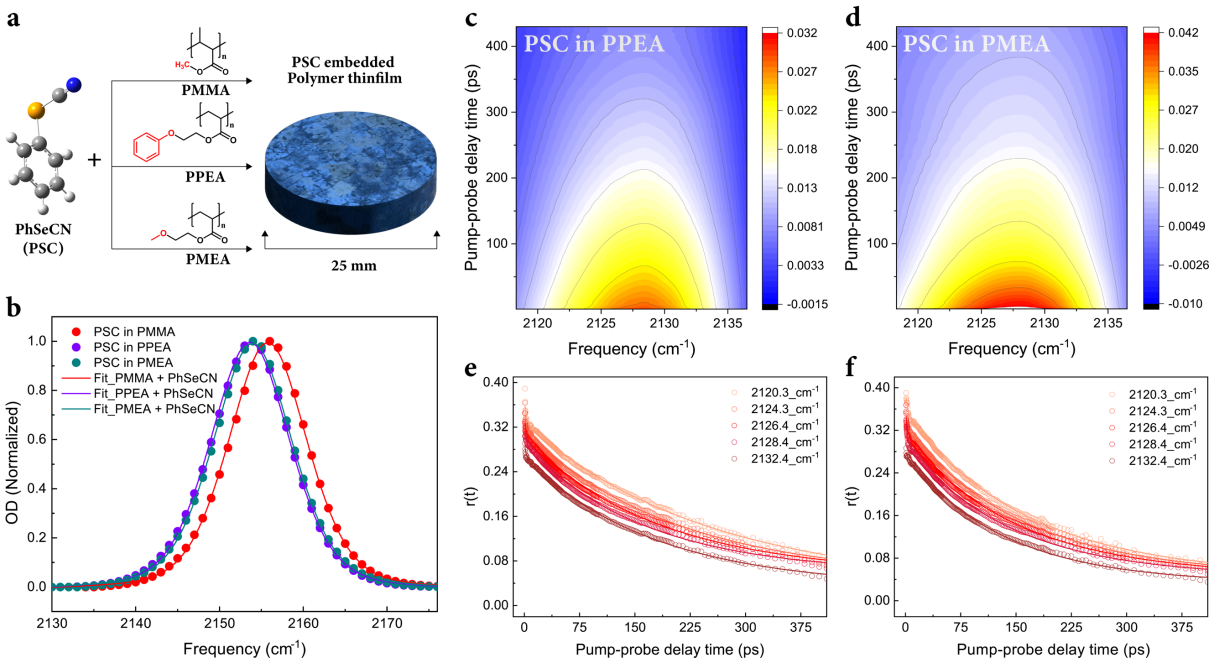

Figure 5. (a) PSC embedded PMMA, PPEA and PMEA thin-film. (b) Background subtracted and normalized FT-IR spectra of the CN band of PSC in PMMA (red), PPEA (violet), and PMEA (dark cyan), DWT-corrected isotropic IR-PP signal of PSC in PPEA (c) and in PMEA (d), and probe frequency-dependent anisotropic IR-PP signal of the CN stretch band of PSC in PPEA (e) and in PMEA (f).

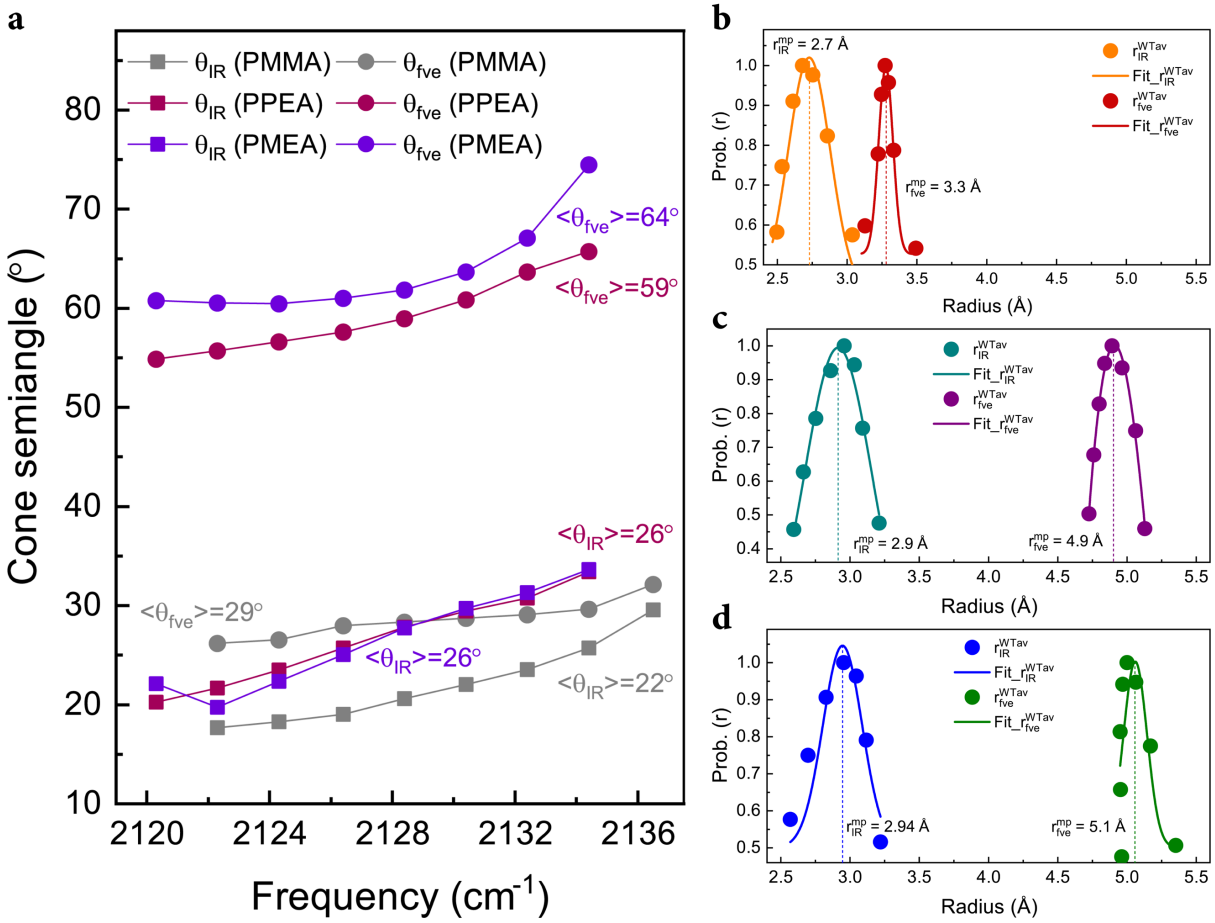

Figure 6. (a) The frequency-dependent distribution of the cone half-angle associated with the internal rotational fluctuation, θ_{IR}, and WIAC motion, θ_{fve} in PMMA (grey), PPEA (maroon), and PMEA (violet) polymer, which shows that they gradually increase with the increase of probe beam frequency. The standard error of the mean in estimating the different cone half angles at any frequency remains $\leq \pm 0.5°$, (b) center-weighted probability distribution of the FVE radius associated with the internal rotational fluctuation of the -SeCN probe about the C(Ph)-Se(CN) bond vector, $P\{r_{IR}(\omega)\}$ and WIAC motion $P\{r_{fve}(\omega)\}$ of (a) PMMA (orange and red circles, respectively, (b) PPEA (dark cyan and purple circles, respectively), and (c) PMEA polymer (blue and olive green circles, respectively), whereas corresponding solid curves represent the fitting lines using the Gaussian function. The significant incrase of the r_{fve}^{mp} can be observed from PMMA to PMEA whereas r_{IR}^{mp} remains similar for different polymers.